Plasma Physics and
Controlled Fusion

PURPOSE-LED
PUBLISHING™

Latest developments in the maximum likelihood tomography for offline and real time analysis of radiation emission in tokamaks

To cite this article before publication: Ivan Wyss *et al* 2026 *Plasma Phys. Control. Fusion* in press https://doi.org/10.1088/1361-6587/ae7542

Latest Developments in the Maximum Likelihood Tomography for Offline and Real Time Analysis of Radiation Emission in Tokamaks

Ivan Wyss[1*], Riccardo Rossi[1], Teddy Craciunescu[2], Michela Gelfusa[1], Pasquale Gaudio[1] and Andrea Murari[3,4] on behalf of JET contributors[§] and EUROfusion Tokamak Exploitation Team[£]

1) Department of Industrial Engineering, "Tor Vergata" University of Rome, Via del Politecnico 1, 00133, Rome, Italy
2) National Institute for Laser, Plasma and Radiation Physics, Măgurele 077126, Romania;
3) Consorzio RFX (CNR, ENEA, INFN, Università di Padova, Acciaierie Venete SpA), Corso Stati Uniti 4, 35127 Padova, Italy
4) Istituto per la Scienza e la Tecnologia dei Plasmi, CNR, Padova, Italy

[§] See the author list of "Overview of T and D-T results in JET with ITER-like wall" by C.F. Maggi et al., to be published in Nuclear Fusion Special Issue from the 29th Fusion Energy Conference (London, UK, 2023)

[£] See the author list of "Progress on an exhaust solution for a reactor using EUROfusion multi-machines capabilities" by E. Joffrin et al. to be published in Nuclear Fusion Special Issue: Overview and Summary Papers from the 29th Fusion Energy Conference (London, UK, 16-21 October 2023)

[*] Corresponding Author: ivan.wyss@uniroma2.it

Abstract: The knowledge of the total emitted radiation is essential for the understanding and control of tokamak plasmas and its relevance is going to be even higher in the next generation of metallic devices. The total radiation is measured with specific detectors called bolometers along defined collection volumes. The local emission from these integrated measurements is obtained with sophisticated tomographic algorithms, which are required to solve very ill-posed inversion problems. The maximum likelihood tomography is one of the most advanced techniques applied to the bolometric tomography in tokamaks. In this work the latest developments of the maximum likelihood algorithm are overviewed. Firstly, a matrix formulation of the algorithm allows reducing the computational times of orders of magnitude, making the approach suitable to real time applications. Two distinct filtering techniques have been developed to regularize the solution and obtain physically meaningful results: one is optimised for real-time control, the other for offline analysis. Both versions are combined with an adaptive procedure, autonomously adjusting the filtering to the radiation patterns; this improvement reduces the requirements in terms of human intervention and contributes to the standardisation of the results. Furthermore, the uncertainty estimation provided by the maximum likelihood for each voxel is improved and validated with systematic Monte Carlo simulations. The performances of the new algorithms are tested with synthetic data and compared with the main methods reported in the literature. The potential of the new algorithms is demonstrated with its application to the measurements of JET bolometry in discharges with a metallic wall, reconstructing the evolution of the emitted radiation in phenomena such as MARFE, temperature hollowness and disruptions.

Keywords: Radiation, Tomography, Inversion methods, Disruptions, Bolometry, SXR, Maximum likelihood, X Point Radiator, MARFE.

1 Radiation emission and tomography in tokamaks

The measurement of the radiation emitted by tokamak plasmas is crucial for both control and physics studies. Radiation represents an energy loss, and its knowledge is essential for power balance assessments. Localized plasma cooling can lead to anomalies in electron temperature, such as hollowness in the core, thereby causing instability and, eventually, disruptions [1]. Therefore, understanding whether the plasma is emitting anomalously and from which region is essential to take appropriate countermeasures to avoid disruptions [2], [3], [4]. The presence of impurities also contributes to radiation emission (in addition to bremsstrahlung and

cyclotron radiation from the main plasma), so having information about the emitted power can help to obtain a better understanding of transport phenomena [5]. Moreover, different radiative scenarios are being studied to reduce the thermal load on the plasma facing components [6]. For these reasons, many experiments are conducted in different machines with the aim of controlling the impurity seeding and X point radiating regimes [7], [8], [9]. So reliable information on the evolution of the radiative phenomena in these discharges is fundamental in the perspective of the reactor.

Many radiation measurements in tokamaks, such as Soft X-rays or bolometric measurements, do not provide spatially resolved information but only spatial-integrated data. This means that to obtain local information, tomographic inversion must be performed. Tomography, as applied in various scientific fields, often presents substantial challenges, because it aims at solving an inverse problem, in which a set of integrated measurements is utilized to reconstruct a spatial field. In nuclear fusion machines, the difficulties are particularly severe, given the patterns of radiation to be resolved and the limited coverage of the plasma cross-section. In such settings, the problem is normally ill-posed, since the number of unknown parameters exceeds significantly the number of measurements. Consequently, the solution is typically neither unique nor continuous (even minute errors in the acquired measurements can propagate into significant deviations in the reconstructed spatial field), complicating the interpretation of the results. Converging on physically meaningful solution therefore requires the introduction of regularization functions *a priori*. These regularization functions play a crucial role in obtaining reconstructed fields compatible with the underlying physics of the phenomena under investigation.

Different approaches are used in nuclear fusion to obtain tomographic reconstructions [10]. One of the most well-known and utilized techniques is the Tikhonov method, where a regularization function is introduced to stabilize the inversion. A variant of this technique is the Minimum Fisher Regularization, where the regularization is updated at each iteration to minimize the Fisher information [11]. A method, applied in various reactors such as ASDEX Upgrade, is Gaussian process tomography [12]. This approach is conceptually Bayesian and can therefore provide confidence intervals in the reconstructions; the algorithm can also be deployed in real time. Another technique that has produced good results is the Maximum Likelihood Expectation-Maximization (ML-EM). This method is frequentist in inspiration and is based on maximizing the likelihood of the measurements; it can also provide an estimate of the uncertainties in the results, without recourse to delicate Monte Carlo simulations. Various previous works on tomography using ML-EM showed the ability to converge on good reconstructions [13]; however, computational times were of the order of seconds per time slice [14]. In this paper various original improvements to the ML-EM method are presented, to improve accuracy, uncertainty evaluation and computational times.

First a matrix formulation of the algorithm allows a reduction of the computational time of orders of magnitude. Two distinct filtering techniques have been developed to regularize the solution and obtain physically meaningful results. They are called inter-updating filtering because they can be applied between two subsequent iterations of the inversion algorithm. One of these approaches is based on the convolution with a Gaussian filter and the other on anisotropic diffusion. The former provides good results without the information about the magnetic topology, rendering the algorithm suitable for real time applications; the latter is meant to improve the performances of the method for off-line analysis. Moreover, these inter-updating filtering alternatives allow taking into account prior knowledge available if appropriate. On the other hand, to adaptively determine the strength of diffusion, a criterion is proposed and integrated into an automated updating strategy, which can be run without manual intervention. In this way the algorithms self-tune to the radiation emission, improving not only the quality of the outputs and the flexibility of the method but also contributing to the standardisation of the solutions. A detailed analysis of the uncertainties in the obtained reconstructions has also been performed and validated with a systematic set of Monte Carlo simulations.

The performances of the various developed improvements have been investigated with a series of numerical tests based on synthetic data. The potential of the devised algorithms to handle real data is proved with experimental cases from JET. Interesting evidence has been collected about various events such as MARFEs, temperature hollowness and disruptions. It should also be remembered that JET is a particularly relevant machine in this context, not only because of the importance of its experimental programme but also for the

extrapolation to the next generation of devices. Indeed, it is unlikely that future tokamaks will have many fewer lines of sight and a much worse coverage than the bolometric diagnostic on JET. ITER for example will be equipped with a much better bolometric system. The obtained results can therefore be considered a worst case scenario in this perspective.

The paper is organised as follows. In Section 2, the fundamentals of the maximum likelihood are provided, together with a detailed description of the mathematics behind the improvements of the algorithm developed in the present work. A brief overview of the most popular techniques reported in the literature is provided in Section 3. The performances of the different versions in terms of accuracy and uncertainty estimation are evaluated with a systematic series of tests performed with synthetic data in Section 4. The potential of the proposed upgrades of the method to handle experimental data is the subject of Section 5. In section 6, the prospects of the new approaches in terms of both computational performances and feedback control potential are presented. Conclusions and lines of further investigations are the subject of the last section of the paper.

2 The Maximum Likelihood approach to tomography: background and improvements

This section discusses the main mathematical aspects behind the improvements proposed in the present work. Subsection 2.1 provides the background to the Maximum Likelihood Expectation Maximization algorithm. The matrix formulation of the problem, implemented to reduce the computational times, is presented in Subsection 2.2. The inter-updating filtering is the subject of Subsection 2.3, while the improved approach to estimating the uncertainties in the reconstructions is described in Subsection 2.4.

2.1 The Maximum Likelihood Expectation maximization method

The Maximum Likelihood Expectation Maximization algorithm (ML-EM) stands as a well-established method for the reconstruction of emission tomography [15]. The robustness of ML-EM can be attributed to its ability to handle ill-posed problems [15]. By iteratively refining the emissivity estimate on the basis of the available measurements, ML-EM mitigates the inherent challenges posed by the ill-posed nature of the tomography reconstruction. In the context of nuclear fusion, ML-EM proves particularly advantageous, providing a reliable framework for reconstructing emissivity distributions even in scenarios with limited observation coverage [16], [17].The other positive aspect of the technique is its capability of routinely estimating the confidence intervals in the final reconstruction, without making recourse to demanding and delicate Monte Carlo routines [16], [18]. Moreover the method can handle well artefacts due to toroidal asymmetries in the emitted radiation and the specific layout of JET bolometic system (see Subsection 4.3).

The fundamental principle underlying this approach is to maximize the conditional probability of obtaining a specific set of measurements, denoted as g, given the emissivity f.

$$L(g|f) = \prod_m L(g_m|f) \tag{1}$$

Where m indicates the generic measurement (line integral). Such an objective requires maximizing an objective function, which can include a regularization term U solely dependent on the emissivity f:

$$f_{ML} = argmax[L(g|f) - U(f)] \tag{2}$$

It can be demonstrated that it is possible to find a solution to equation (2) with a preconditioned gradient ascend algorithm, implementing the following iterative formula:

$$f^{k+1} = f^k + \alpha C^k(f^k)\left[\nabla_f L(g|f) - \nabla_f U(f)\right]_{f=f^k} \tag{3}$$

where α is the step size, and C is the preconditioner, a filtering operator. It is normally assumed that the raw data are Poisson random variables [15], [16].

The problem is typically formulated in discrete form by dividing the plasma cross section in toroidally symmetric small volumes (called voxels in the rest of the paper). In compact form, the relationship between the emissivity f_n of the voxels and the measurements g_m can be written as:

$$g = Hf \tag{4}$$

Where H is the sensitivity matrix that, from the geometry of the diagnostic, encodes the contribution of the radiation emitted by the jth voxel to the ith measurement. Mathematically speaking, the ill-posed character of the inversion task is due to the fact that the matrix H is not invertible.

The log-likelihood of a generic Poisson distribution is:

$$L(g|f) = \sum_i g_i \log \bar{g}_i - \bar{g}_i - \log g_i! \tag{5}$$

Where $g_i!$ is the factorial of g and $\bar{g}_i$ is the mean value of the measurement of the ith detector.So the derivative of this with respect to f can be written as

$$\nabla_f L(g|f) = H' diag[Hf]^{-1} g - s \tag{6}$$

In equation (6) $s=H'1$, where H' is the transpose of the matrix H and 1 is a vector, whose entries are all set to 1. Substituting in equation (3), considering a typical preconditioner such as $\alpha C^k(f^k) = diag[f^k] diag[s^{-1}]$, and excluding the regularization term $U(x) = 0$, one obtains:

$$f^{k+1} = f^k + diag[f^k] diag[s^{-1}](H' diag[Hf]^{-1} g - s) \tag{7}$$

Which leads to

$$f^{k+1} = diag[f^k] diag[s^{-1}](H' diag[Hf]^{-1} g) \tag{8}$$

From equation (8), for each voxel we can write an iterative algorithm, which converges to the maximum likelihood estimation:

$$f_n^{k+1} = \frac{f_n^k}{s_n} \sum_m \frac{g_m}{\sum_j H_{mj} f_j^k} H_{mn} \tag{9}$$

Where f_n^k is the emissivity of pixel n at iteration k and s_n is just a normalisation factor. Equation (9) is one of the most used expressions for implementing the maximization of the likelihood, as described in [17]. As demonstrated in [19], the iterative algorithm can be adapted and performs very well even if the measurements do not present a Poisson distribution. More importantly for the subject of the present paper, equation (9) is an iterative formula for each of the n voxels; its implementation requires nested loops for the voxels and lines of sight and therefore it is very heavy in terms of computational time, which is not necessarily an issue for medical applications, but it is in fusion, particularly for real time deployment.

2.2 The Matrix formulation of the ML-EM algorithm

Instead of relying on the iterative formula (9), one can directly update the emissivity of all the voxels using the matrix form in equation (8).All the matrixes in equation (8) are diagonal and so their product can be written as the Hadamard product, which for matrixes of the same dimension is

$$(A \odot B)_{ij} = (A)_{ij}(B)_{ij} \tag{10}$$

While for a matrix A of dimensions nxm and an array b of n rows, it becomes:

$$(A \odot B)_{ij} = (A)_{ij}(B)_i \tag{11}$$

So using this product it is possible to rewrite equation (8) as:

$$f^{k+1} = f^k \odot s^{-1} \odot \left(H \left(H' f^k \right)^{-1} \odot g \right) \tag{12}$$

Where the inverse is an element-wise operator

$$(A^{-1})_i = 1/A_i \tag{13}$$

In compact form, equation (12) can be written as [18]:

$$f^{k+1} = \frac{f^k}{s} \left[\frac{H}{H f^k} g \right] \tag{14}$$

It results that equation (14) can be calculated much faster than the more traditional (9) and therefore this is the version implemented to obtain all the results reported in the rest of the paper.

2.3 Inter-updating filtering

The ML-EM algorithm is characterized by slow convergence and tends to produce solutions vulnerable to noise. To address these challenges, regularization or filtering becomes necessary. In [19] the regularization was implemented through an average filtering along closed magnetic surfaces, while for opened magnetic lines a smoothing spline procedure was adopted. Instead of a conventional regularization function U, in the present work a filtering operation denoted by *F* has been introduced. This filtering operation is applied at each iteration, so it is called "inter-updating filtering" (ML-IU) approach. The inter-updating filtering has been implemented with the formula:

$$f^{k+1} = F^k f^k + F^k \alpha C^k(f^k) \left[\nabla_f L(g|f) \right]_{f=f^k} \tag{15}$$

Where *F* is a linear operator such as a convolutional matrix. In this work we have studied two different inter-updating filtering approaches: one with a linear Gaussian kernel and one with anisotropic diffusion along the magnetic field lines.

Gaussian filtering is a very useful and consolidated mechanism primarily to diminish the effects of the noise on the reconstruction process. It allows imposing that the emissivity cannot be discontinue but has to vary smoothly inside the plasma. This refined approach is denoted as ML-GAUSS in the following. It can be implemented without knowledge of the magnetic topology and therefore requires computational times compatible with real time deployment (see Section 6).

For detailed physical studies, in practically all tokamaks, given the layout of the bolometric diagnostics and the complexity of the patterns to be reconstructed, it is indispensable to apply some form of smoothing along the magnetic field lines, to obtain accurate 2D emissivity maps. Anisotropic diffusion, a well-established approach in image reconstruction, is a very powerful technique for smoothing along vector fields [20], [21]. The main idea relies on the fact that solving the following PDE of the following diffusion equation (16) is equivalent to smoothing with a Gaussian filter as demonstrated in [20]:

$$\frac{\partial f}{\partial \lambda} = D \nabla^2 f \tag{16}$$

Where *f* is the reconstructed emissivity field and *D* is the diffusivity coefficient. The solution of (16) is a function of a time-like variable λ, $f(\lambda)$, where larger λ corresponds to wider diffusions and can be written as

$$f(\lambda) = f(\lambda = 0) * G(\lambda) \tag{17}$$

Where G is a Gaussian kernel filter operator, with the variance σ that is dependent on the time-like variable λ. So, the smoothing properties are determined by the diffusivity coefficient *D* and λ. In the present application, λ is to be interpreted as a simple smoothing parameter and not time. Indeed it determines the variance of the Gaussian function applied to the individual time slices of the reconstructions. In more detail, the algorithm

implements the integral version of (17) and solving a diffusion equation always requires integrating along a "time" variable, which in the present case simply controls the amount of smoothing by acting on the variance of the Gaussian kernel filter G.

In case of a different PDE, where the Laplacian is oriented along two unitary orthonormal vectors u_t and u_n, the solution leads to a 1D Gaussian smoothing process along those directions with weights β_t and β_n. In such a case equation (16) can be rewritten as:

$$\frac{\partial f}{\partial \lambda} = \beta_t \frac{\partial^2 f}{du_t^2} + \beta_n \frac{\partial^2 f}{\partial u_n^2} \tag{18}$$

This means that solving equations (18) is equivalent to smoothing with an oriented Gaussian kernel, as reported in [21].This provides a simple way of smoothing an image f along a generic vector field, such as a magnetic field, by defining u_t as the unitary vector tangent to the magnetic field and u_n to the normal one. As reported in Figure 1 for a generic image, higher values of λ result in larger smoothing. Furthermore, in principle the definition of the vector field can help implement a different smoothing depending on the region of the cross section.

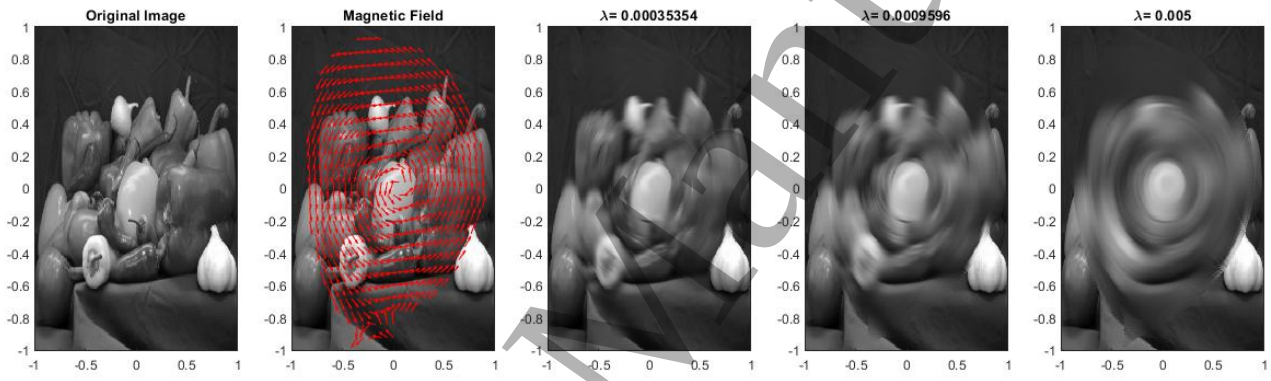

Figure 1: Dependence of the smoothing on the parameter λ of the anisotropic diffusion. Laplacians are oriented along a generic magnetic equilibrium of JET. The arrows in the second plot are just meant to guide the eye: since the filtering is implemented as a convolution, the results do not depend significantly on the sense of rotation (clock or anticlockwise).

This method is clearly effective for smoothing along the magnetic lines, but the strength depends on the value of the time-like variable λ. For this reason, an adaptive routine, which automatically determines the best diffusion strength, has been developed. The central concept of this inter-updating filtering approach, called ML-DIFFUSE, is to smooth iteratively the ML-EM solutions by solving the diffusion equation. In essence, assuming a constant diffusion coefficient across the entire cross-section, the PDE of the diffusion is then applied to the emissivity f_{ML} provided by the iteration of the maximum likelihood algorithm. At each iteration of the ML-EM algorithm, the solution converges on an $f_{ML,}$ which is used as initial condition in the diffusion equation. Then the value of λ is progressively reduced while the right solution is approached. Different methods for updating the value of λ are possible. The one adopted, to obtain the results reported in the rest of the paper, is based on the residuals, which are the differences between the measurements (experimental or synthetic) and the reconstructions. It consists of dividing in half the interval when the Root Mean Square Error (RMSE) of the residuals reaches a plateau, in particular when the variation between two consecutive iterations is less than 0.5%. The iterations are halted when a suitable stop condition is met. This self-tuning is essential to reduce human effort and to standardise the solutions. It can also help identify new radiation patterns as discussed in Sections 4 and 5. The ML-DIFFUSE algorithm is described graphically in the flowchart of Figure 2. It is worth mentioning that, in the present implementation, the tuning of the lambda is independent from the estimated uncertainties. However further developments could profit from the uncertainty estimation to optimise the updating factor λ.

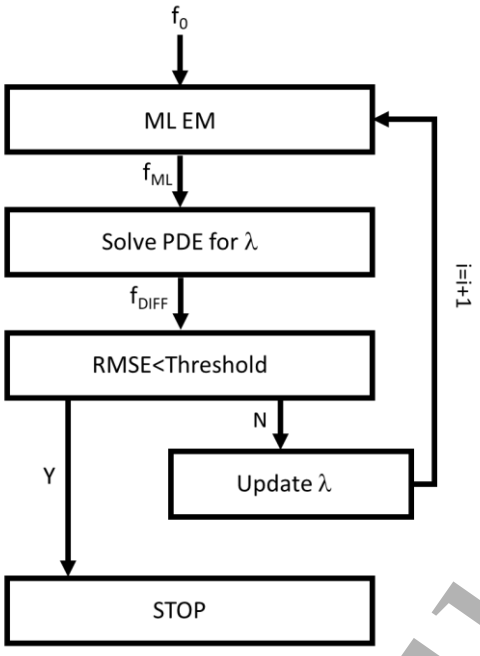

Figure 2: Flow chart of ML Diffuse adaptive strategy with i indicating the iteration number.

2.4 Uncertainty estimation

To provide an estimate of the uncertainties in the final reconstructed emission, it is necessary to quantify how the noise in the measurements propagates in the reconstruction process. To address this aspect, an approach to uncertainty analysis was introduced in [22].

The objective of the inversion algorithm consists of estimating the 2D image f by maximizing an objective function as expressed in equation (2). Let us suppose that the measurements are affected by the noise n and let us indicate with ε^k the uncertainty in the image estimation at iteration k:

$$f^k = \overline{f^k} + \varepsilon^k \tag{19}$$

$$g = \bar{g} + n \tag{20}$$

Where $\overline{f^k}$ and $\bar{g}$ are the expectations of the image and measurements respectively. An expression can be derived for the expectation $\bar{f}^k$ and the noise evaluation ε^k separately, assuming small absolute errors:

$$\bar{f}^{k+1} = \bar{f}^k + \alpha C^k(\bar{f}^k)\left[\nabla_f L(\bar{g}|\bar{f}^k) - \nabla_f U(\bar{f}^k)\right] \tag{21}$$

$$\varepsilon^{k+1} = [I - A^k]\varepsilon^k + B^k n = V^{k+1} n \tag{22}$$

In equations (21) and (22) A and B can be written as

$$A^k = -\alpha C^k(\bar{f}^k)\left[\nabla_{ff} L(\bar{g}|\bar{f}^k) - \nabla_{ff} U(\bar{f}^k)\right] - \alpha M\left[\nabla_f L(\bar{g}|\,\bar{f}^k) - \nabla_f U(\bar{f}^k)\bar{f}^k\right] \tag{23}$$

$$B^k = \alpha C^k(\bar{f}^k)\nabla_{fg} L(\bar{g}|\bar{f}) \tag{24}$$

Where M is a matrix where the (j,l) element is $\sum_m g_m \partial C^k_{j,m}/\partial f_l$ and its evaluation is strictly related to the preconditioner. In its turn the variance V can be written as:

$$V^{k+1} = [I - A^k]V^k + B^k \tag{25}$$

Then the covariance of the reconstructed image is

$$\Sigma_{f^k} = V^k \Sigma_g [V^k]' \tag{26}$$

Where Σ_g is a sum over the lines of sight. The term A depends on the conditioner C, the regularization, and the likelihood, and so has to be evaluated specifically for each problem. Equation (26) is used to estimate the uncertainties, which are the diagonal elements of the covariance matrix. In the case of emission tomography, assuming Poisson data and that the errors are small compared to the useful signal, recalling equation (5) one can derive

$$\nabla_{ff} L(g|f) = -H' diag[Hf]^{-2} diag[g] H \tag{27}$$

$$\nabla_{fg} L(g|f) = H' diag[Hf]^{-1} \tag{28}$$

Then, combining equation (27) and (28) with (23) and (24), it is possible to write:

$$A^k = diag[f^k] diag[s^{-1}] H' diag[Hf^k]^{-2} diag[\bar{g}] H - diag[f^{k+1}] diag[f^k]^{-1} + I \tag{29}$$

$$B^k = diag[f^k] diag[s^{-1}] H' diag[Hf^k]^{-1} \tag{30}$$

As reported in [18], [22], assuming a fast convergence of the ML algorithm, we can write:

$$A^k = diag[f^k] diag[s^{-1}] H' diag[Hf^k]^{-1} H \tag{31}$$

Using again the compact notation fort the Hadamard product, it is possible to simply reformulate A and B as:

$$A^k = \frac{f^k}{s\, Hf^k} H' H \tag{32}$$

$$B^k = \frac{f^k}{s\, Hf^k} H' \tag{33}$$

Finally, in case linear updating is adopted, the expression (25) becomes:

$$V^{k+1} = F^k [I - A^k] V^k + F^k B^k \tag{34}$$

Where A and B are the ones defined previously in (23) and (24). This last expression is fundamental in this work for evaluating the uncertainties of the inter updating filtering approach. Indeed, for ML-GAUSS *F* is the linear convolutional matrix of the Gaussian smoothing. It is worth noting that in a maximum likelihood with an inter-updating filtering algorithm, in which a smoothing is applied, utilizing equation (25) and then smoothing the variance is totally different from and less mathematically sound than using equation (34). On the other hand, equation (34) is only valid for linear inter updating and so the error cannot be evaluated if a nonlinear operator is utilized. However, thanks to the equivalence between solving the PDE and applying Gaussian oriented smoothing, which is a linear operator, the expression (34) remains valid also for the ML-DIFFUSE algorithm.

3 Brief overview of the most utilised inversion algorithms.

In the field of nuclear fusion, various methods have been developed to provide 2D tomographic reconstructions from bolometric measurements [23]. One of the most commonly used alternatives implements the Tikhonov regularization, where an objective function ϕ of the following form is minimized:

$$\phi = \left| |Hf - g| \right|^2 + \alpha R \tag{35}$$

In the previous formula, the first part is the fidelity term and represents the proximity to the measurements, while R is a regularization function that can take different forms. One possibility is to use linear regularization that minimizes the gradient of the emissivity:

$$R = f_x + f_y \tag{36}$$

Where f_x and f_y are respectively the derivatives of the emissivity along x and y. Another solution can be to minimize the curvature of the emissivity, and in that case:

$$R = f_{xx} + f_{yy} \tag{37}$$

Obviously, since the emissivity depends on the magnetic topology, another solution is to minimize the curvature of the emissivity along the magnetic field lines. So one of the most used regularisation terms in this approach, and also adopted in the present work, is:

$$R = \frac{\partial^2 f}{\partial u_t^2} + \frac{\partial^2 f}{\partial u_n^2} \tag{38}$$

Where u_t and u_n are the directions respectively parallel and orthogonal to the magnetic field.

Another often-used technique is Minimum Fisher Regularization (MFR). The idea is to minimize the Fisher information:

$$I_F = \int \frac{g(x)'^2}{g(x)} dx \tag{39}$$

where the apostrophe indicates a derivative with respect to x. A way to obtain the minimization, as suggested in [11] , is to use a weighted regularization function, whose weights are updated iteratively so that

$$R = W^n \left(\frac{\partial^2 f}{\partial u_t^2} + \frac{\partial^2 f}{\partial u_n^2} \right) \tag{40}$$

Where W is defined as

$$W^n = \frac{1}{f^n} \; if \; f^n > 0 \tag{41}$$

$$W^n = W_{max} \; if \; f^n < 0 \tag{42}$$

It has been shown that after few iterations, the solution converges to the one with the minimum Fisher information.

4 Investigating the potential of the improved ML-EM algorithm with synthetic data.

In this section, a comprehensive examination of the performance of the two inter-updating filtering approaches, ML-GAUSS and ML-DIFFUSE, is reported. This evaluation is performed with synthetic data, also called phantoms and representing the main radiation patterns encountered in practice in metallic tokamaks. By construction, the phantoms are quite challenging to reconstruct. Indeed, their intensity changes abruptly from zero to the reported value in the space of single voxel. Their edges are therefore more precipitous than in reality and also beyond the spatial resolution of JET diagnostic (see later). To simulate also the experimental errors, unless differently specified, a Gaussian noise of amplitude equal to 10% of their amplitude has been added to the synthetic line integrals. The two developed approaches, ML-DIFFUSE and ML-GAUSS, are examined

also to assess their capability to properly estimate the uncertainties in the final output. The investigation includes a comparison with the other most used tomographic algorithms, to confirm the quality of the obtained results.

For these numerical tests, and not only for the experimental cases described in Section 5, the analysis is particularised for JET bolometric diagnostic. The bolometer system of JET comprises two cameras, one positioned vertically and the other horizontally, each equipped with 24 lines of sight (LOS)[24], as depicted in Figure 3. The implementation of the present work includes the actual geometry of the viewing cone for each line of sight. The rectangular grid implemented consists of 5782 voxels, with 3565 voxels situated inside the vessel. It is worth noting that these grid dimensions are of the order of magnitude typical of modern tokamaks, given the constrained view of the collecting geometry. The limited angles of observation inherent in such systems necessitate a careful optimisation of the reconstruction algorithm, making the comparison and evaluation presented in this section particularly relevant to practical applications.

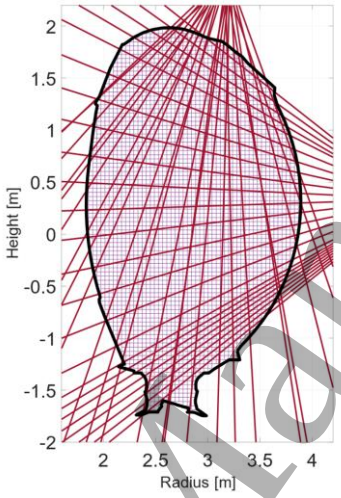

Figure 3: JET Bolometer Lines of Sight. In the poloidal cross-section, the voxels used for the reconstructions in the present work are reported.

The present section is structured as follows. Subsection 4.1 describes the results of the regularization through linear filtering with a Gaussian kernel. The performances of the anisotropic diffusion with an adaptive procedure is the subject of Subsection 4.2. The next Subsection 4.3 is devoted to a study of artefacts consequence of the fact that the two cameras are not in the same toroidal location. Finally a brief comparison of the developed algorithms with the techniques most utilised in the community is reported in Subsection 4.4.

4.1 Gaussian Filtering

In the following, Subsection 4.1.1 documents the accuracy of the inter-updating algorithm with the Gaussian filter and in Subsection 4.1.2 its reliability in estimating the confidence intervals in the reconstructions is tested with a Monte Carlo approach.

4.1.1 Gaussian inter-updating (ML-GAUSS): reconstruction quality

In the ML-GAUSS algorithm, at each iteration the image is convolved with a Gaussian kernel filter of fixed sigma. In this work the parameters of the Gaussian kernel are sigma equal to 1 and window size of 3x3 voxels. This choice introduces a stabilizing effect, rendering the method less influenced by the initial conditions as exemplified by the two cases shown in Figure 4. A crescent shape phantom on the low field side is reconstructed starting with two completely different first guesses. Remarkably, for both initial conditions, this approach yields the same solution. Such robustness is a very significant advantage in devices such as JET, with an extremely varied experimental programme, resulting in very different radiation patterns.

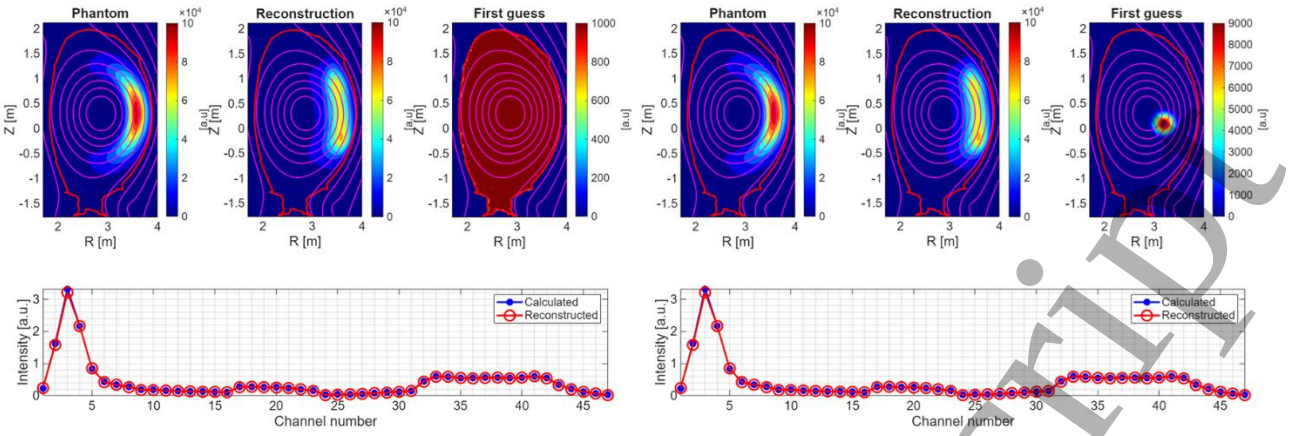

Figure 4: ML-GAUSS reconstructions starting from two different first guesses. Left plots: the phantom to be reconstructed. Middle plots: the final reconstructions. Right plots: the initial guesses. Bottom: comparison of the synthetic and reconstructed projections. Since the projections are perfectly reconstructed, the differences between the phantoms and the final outputs are to be attributed to the limitations of the diagnostic layout and not to the inversion algorithm.

Another very important point to notice is that the present implementation of the inter-updating with the Gaussian filter algorithm does not require information about the magnetic topology. This is an additional added value in the perspective of real time implementations (see also Section 6).

4.1.2 ML-GAUSS: test of the error propagation with a Monte Carlo approach

The objective of this subsection consists of analysing the error propagation of the technique. To this end, a Monte Carlo type of approach has been implemented. As depicted in Figure 5, a crescent shape phantom is placed on the low field side, and from it, the expected measurements have been calculated. Subsequently, Gaussian noise with a variance σ is added to these measurements. Then, these noisy measurements have been used as input to 100 reconstructions with ML-GAUSS. The average of these reconstructions has then been compared with the single reconstruction obtained with the averaged measurements as inputs. From Figure 5, it is evident that the averaged reconstructions and the reconstruction of the averaged measurements coincide. This observation, confirmed by the analysis of other phantoms of different shape, proves the stability and consistency of the ML-GAUSS algorithm, showcasing its capability to yield reliable and robust reconstructions even under noisy measurement conditions.

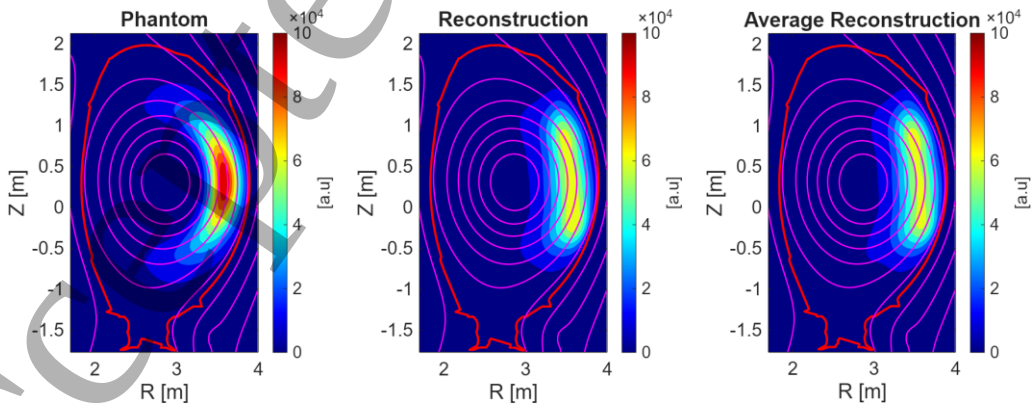

Figure 5 : (Left) Phantom. (Middle) Reconstruction of the averaged measurements. (Right) Average of the individual reconstructions

The direct evaluation of the variance calculated with the propagation equation (34) is shown in Figure 6, where it is compared with the corresponding variance of the 100 individual reconstructions (called Monte Carlo MC in the figure). A notable trend observed is the levelling of the variances as the number of reconstructions

increases. This means that few iterations are required to obtain a good convergence to the correct uncertainty estimate. Consequently, for real time applications the accuracy obtained after 15÷20 iterations is typically sufficient (see Section 6).

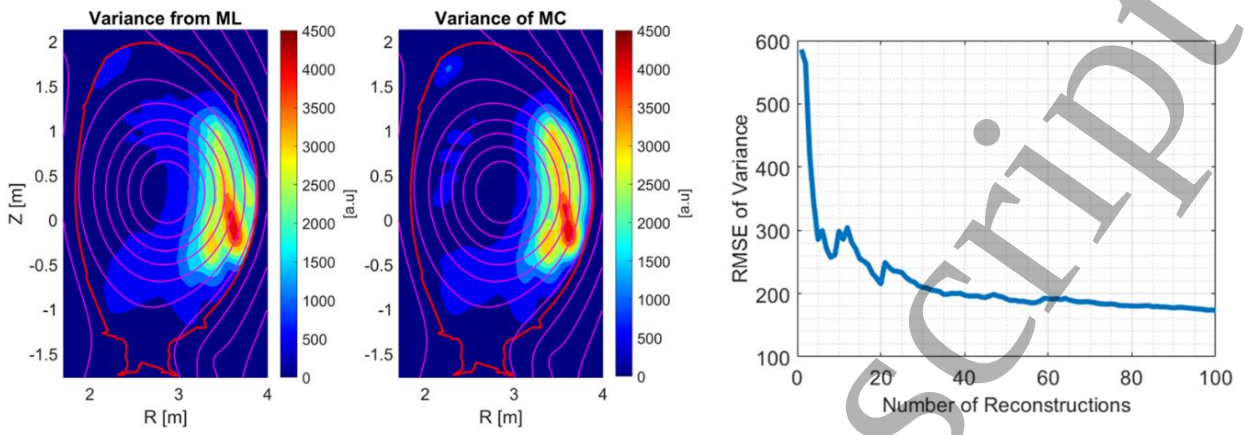

Figure 6 : (Left) The final variance of the image evaluated from equation (34). (Middle) The final variance of the MC approach. (Right) RMSE of the variance versus the number of the reconstruction.

4.2 Anisotropic diffusion

This section describes the performances of the algorithm implementing the adaptive anisotropic convolution, ML-DIFFUSE. Subsection 4.2.1 is devoted to the analysis of the algorithm accuracy, while the estimate of the confidence intervals is verified with Monte Carlo simulations in Subsection 4.2.2.

4.2.1 Anisotropic diffusion inter-updating (ML-DIFFUSE): reconstruction quality

As described in Subsection 2.3, the algorithm with inter updating based on anisotropic diffusion progresses in two phases. In the first phase the ML-EM is run to identify the regions, in which the main radiation is localised. Subsequently, in the second phase, the anisotropic diffusion equation is run utilizing the output of the previous phase as first guess. The integration of updating and filtering processes forces the ML-EM algorithm to converge more stably toward a single solution. Recursive filtering provides an additional layer of stabilization, allowing for the introduction of prior conditions that the solution should adhere to. Notably, a linear filter typically relies on various parameters, whose determination is a critical aspect. In this algorithm, these parameters are dynamically and autonomously tuned throughout the reconstruction. This adaptive automatic tuning enhances the flexibility and adaptability of the inter-updating filtering approach, making it well-suited to diverse reconstruction scenarios and contributing to the overall robustness of the algorithm.

To show the importance of the smoothing parameter on the solution, the inter-updating filtering with anisotropic diffusion has been run with a fixed value of the diffusion step λ. In Figure 7 the reconstructions obtained with three different λ values are reported for the phantom of Figure 5. As understandable, the algorithm converges to slightly smoother solutions for larger values of the hyper-parameter λ. In the bottom of Figure 7 the respective errors for reconstructions and lines of sights are shown. All the three reconstructions converge on different solutions after a certain number of iterations. The smallest error is reached using a value of λ equal to 0.01, which results in a better fit of the phantom.

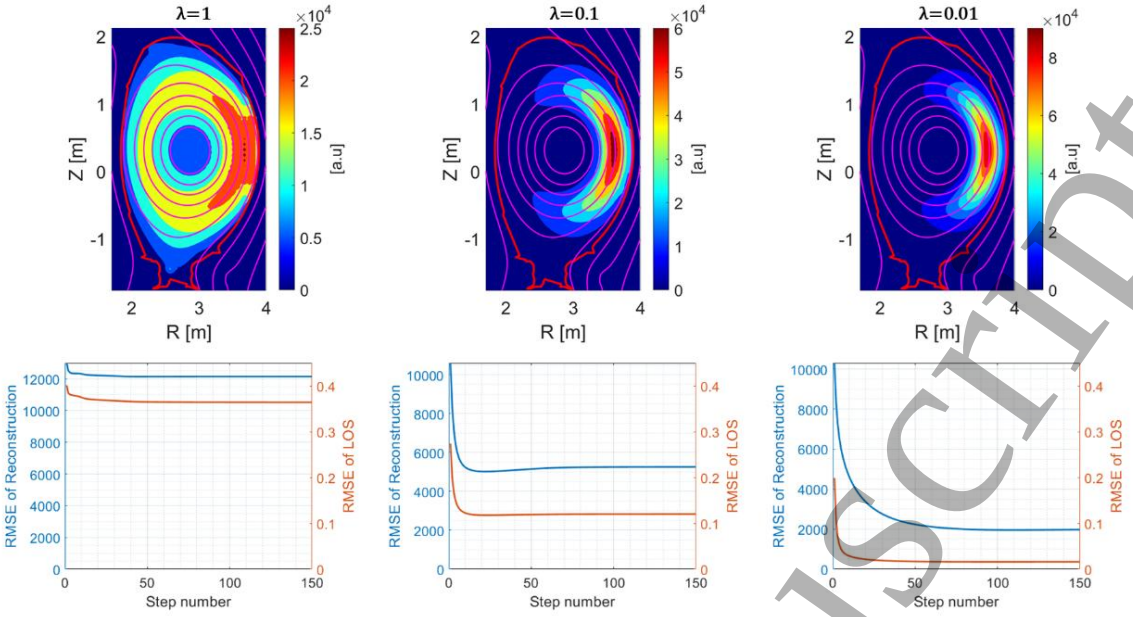

Figure 7: Three different ML-DIFFUSE reconstructions, with different but fixed smoothing values of the hyper-parameter.

In this context determining the optimal λ value is fundamental. The adaptive strategy, implemented in this work, consists of starting with a large value of this hyper-parameter and reducing it when the RMSE of the difference between the original and reconstructed LOS reaches a plateau. In particular, when in two consecutive iterations the relative variation is less than 0.005, the λ is divided by half. The evolution of the RMSE and the results of the iterative process are shown in Figure 8 for two completely different emission patterns.

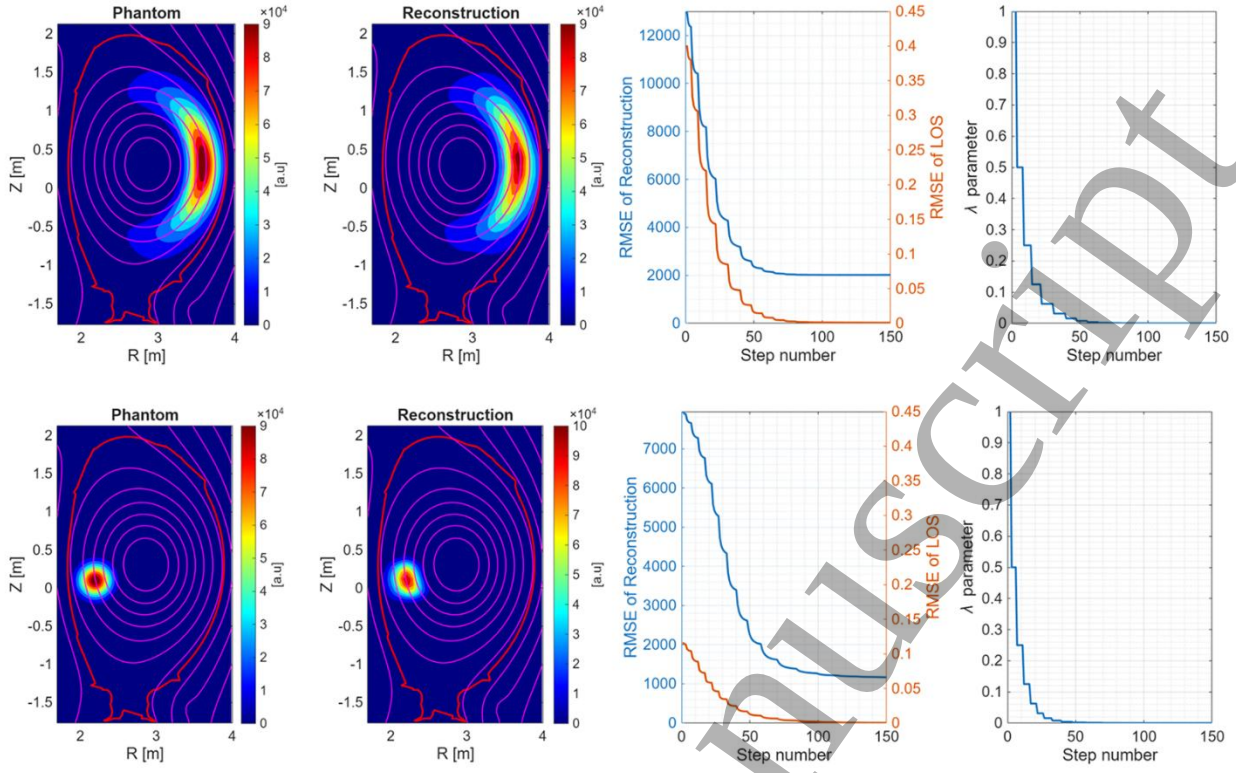

Figure 8: Left: Original phantom. Middle: Final reconstruction. Right plots: RMSE of LOS and reconstruction at different iterations. The two right plots report the evolution of the hyper-parameter λ.

After fewer than 50 iterations, the obtained solutions show a very good agreement with the phantoms, as depicted in Figure 8. This alignment is attributed to the inherent smoothing effect along the magnetic lines implemented by the algorithm. The iterative inter-updating filtering with variable values of the hyper-parameter λ, combining the strengths of diffusion and ML-EM, contributes to the convergence of the solution on a representation that agrees very well with the expected characteristics of the emitted region. In Figure 8, the trend of the error in terms of RMSE is shown for both lines of sight and reconstructions. On the right plot, the λ value associated with each step of the algorithm is also depicted. The initial λ value is set to 1, leading to a strongly smoothed reconstruction. After several iterations, the error reaches a plateau, prompting a halving of the smoothing hyper-parameter.

The important point to appreciate is that the devised algorithm converges automatically to any type of realistic radiation pattern. Indeed, the level of smoothing required to resolve a specific pattern would typically produce suboptimal results for a completely different type of radiation emission. A completely inadequate filtering choice could even prevent the identification of unexpected patterns such as the radiation ring discussed in Section 5. This has been demonstrated by applying the algorithm to a series of phantoms representative of all the main radiation patterns detected on JET.

4.2.2 ML-DIFFUSE: test of the error propagation with a Monte Carlo approach

In this section, a comparison between the error evaluated using equation (34) and the one obtained with the Monte Carlo method for the ML-DIFFUSE approach is presented. The reference case is the usual phantom with a crescent shape pattern on the low-field region. However the results and conclusions are fully representative of what can be obtained with all the other typical radiation patterns encountered in practice on JET. The synthetic measurements have been calculated, assuming that they are affected by Gaussian errors with a variance of 10% of their value. Subsequently, from 100 sets of measurements 100 reconstructions have been obtained using the ML-DIFFUSE method. The mean of these reconstructions is then compared with the

reconstruction obtained with the average of the measurements. As in the previous case, the reconstructions are almost the same, as shown in Figure 9.

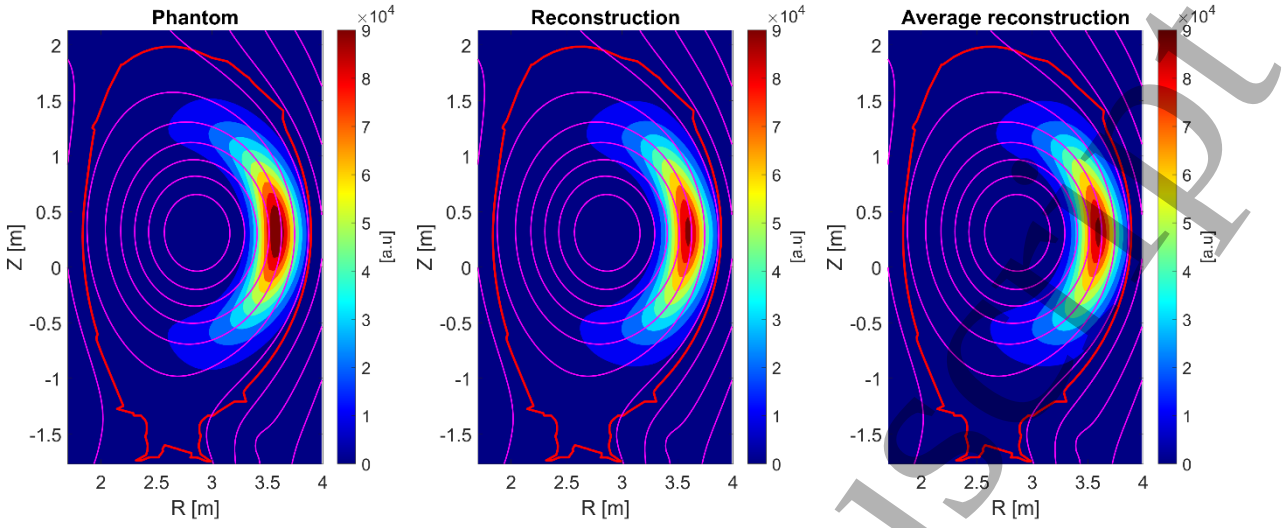

Figure 9: (Left) Low field phantom. (Middle) Reconstruction of the averaged measurements. (Right) Average of the individual reconstructions.

In Figure 10, the variance calculated with equation (34) is compared with the variance evaluated over the 100 reconstructions. As observable in Figure 10(right), the relative error between the two approaches decreases with the number of iterations, indicating that the error assessed through (34) proves to be a good solution for evaluating the uncertainty propagation.

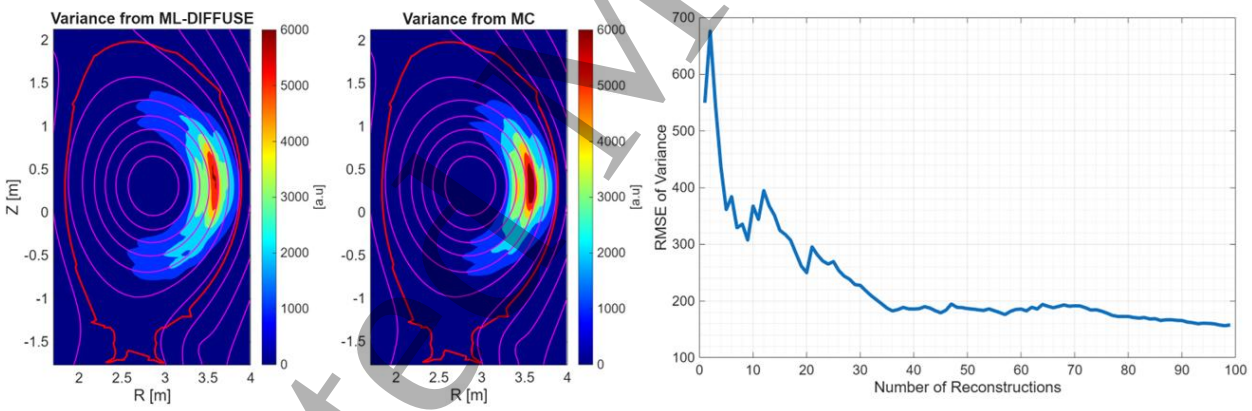

Figure 10: (Left) Final variance of the image evaluated from equation (34). (Middle) Final variance of MC. (Right) RMSE of the reconstruction variance versus the iteration number.

4.3 Artefacts analysis

On JET, the horizontal and vertical cameras are located in different toroidal positions, and therefore observe different poloidal regions. Moreover, the region seen by the vertical camera does not fully overlap with that observed by the horizontal camera, leaving certain areas in the cross-section, such as the upper-left corner,

visible from only one of the cameras, as shown in Figure 11. Consequently, if the radiation exhibits toroidal asymmetries, these limitations of the diagnostic layout can produce artefacts in the reconstructions.

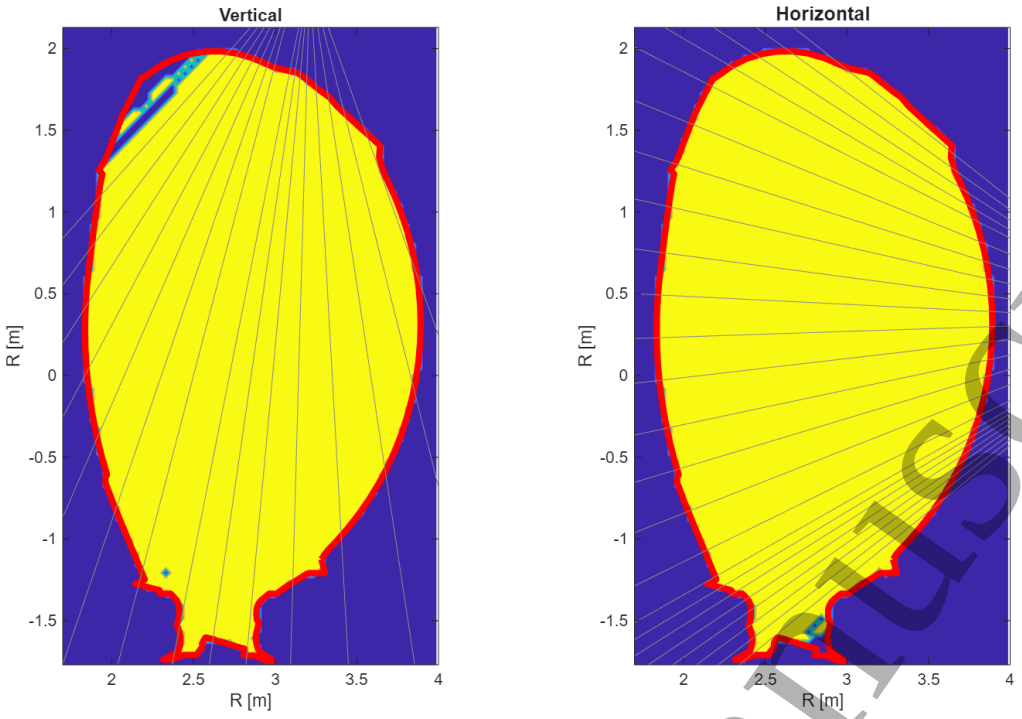

Figure 11: The geometric coverage of the vertical (Left) and Horizontal (Right) camera.

Indeed the aforementioned differences in geometric coverage create a numerically less constrained region, which can be filled with radiation to compensate for the observed asymmetries. This often results in artefacts appearing, for example, in the upper-left corner of the cross-section. To illustrate this, two asymmetric phantom have been generated. In the first the horizontal camera observes a cross-section with 20% more radiation than the vertical camera, see Figure 12 (Top row). This difference leads to a clearly visible artefact in the reconstruction. However, artefacts of such a nature can be detected by analysing the uncertainties in the reconstructions. Indeed the regions where the artefacts are located tend to exhibit unusually higher values of the uncertainty, as shown in Figure 12 for the reported numerical example. The second example exhibits a helical-type asymmetry which can appeared in MARFE, characterized by a toroidally helical radiation structure (Figure 12 bottom row). In a poloidal cross-section, this results in a localized emission appearing at one poloidal angle, while a corresponding structure is observed at a different poloidal angle in another view.

Also in this case the algorithm produces an artefact in the region poorly covered by the lines of sight of the diagnostic. The artefact can be identified by the high value of the uncertainty.

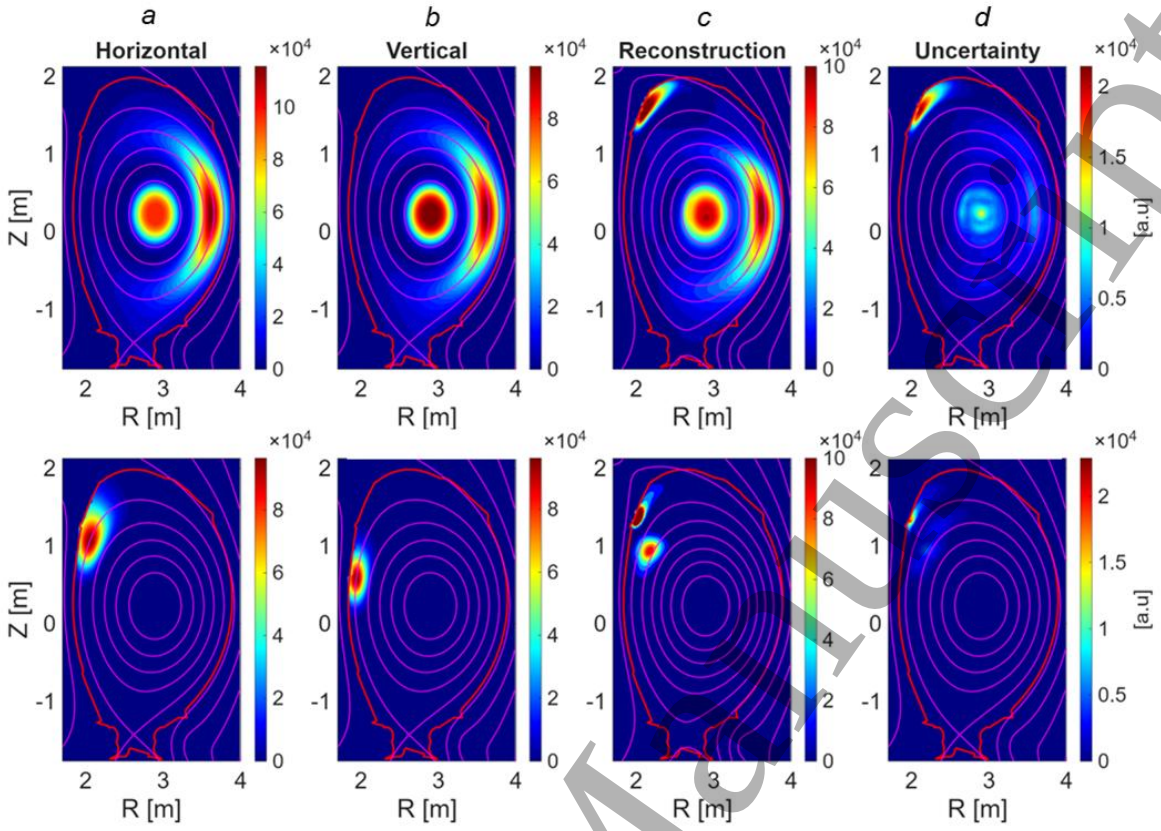

Figure 12 Reconstruction of asymmetric phantoms. (a) Phantom observed by the horizontal camera. (b) Phantom observed by the vertical camera. (c) Reconstruction showing the upper-left artifact. (d) Uncertainty propagation, with higher values highlighting the artifact.

4.4 Estimate of the total radiation for different noise levels

Since both methods estimate the error propagation, it is possible to analyse the impact of the measurement uncertainties on the estimation of emissivity and total power. The analysis has been carried out by attempting to reconstruct the phantom shown in Figure 13 and adding Gaussian noise to the synthetic line integrals with a variance ranging from 0.05 to 0.35. Figure 13 reports also the reconstructions obtained for different noise

variances. Unless otherwise specified, the reported uncertainties have to be interpreted as the 90% confidence intervals.

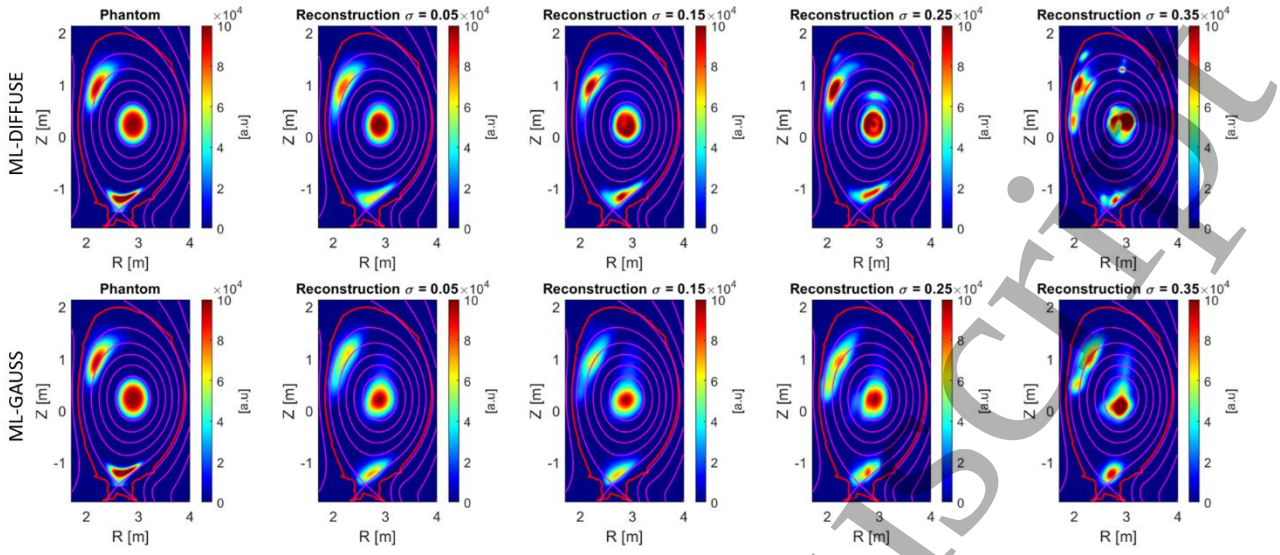

Figure 13: Effect of the measurement uncertainties on the quality of the reconstructions for a quite complex phantom.

As the uncertainty increases, the quality and resolution of the reconstructions progressively degrade, while still preserving good accuracy in localizing the radiation distribution. The impact of the uncertainty in terms of RMSE, evaluated for both methods, is shown in Figure 14.

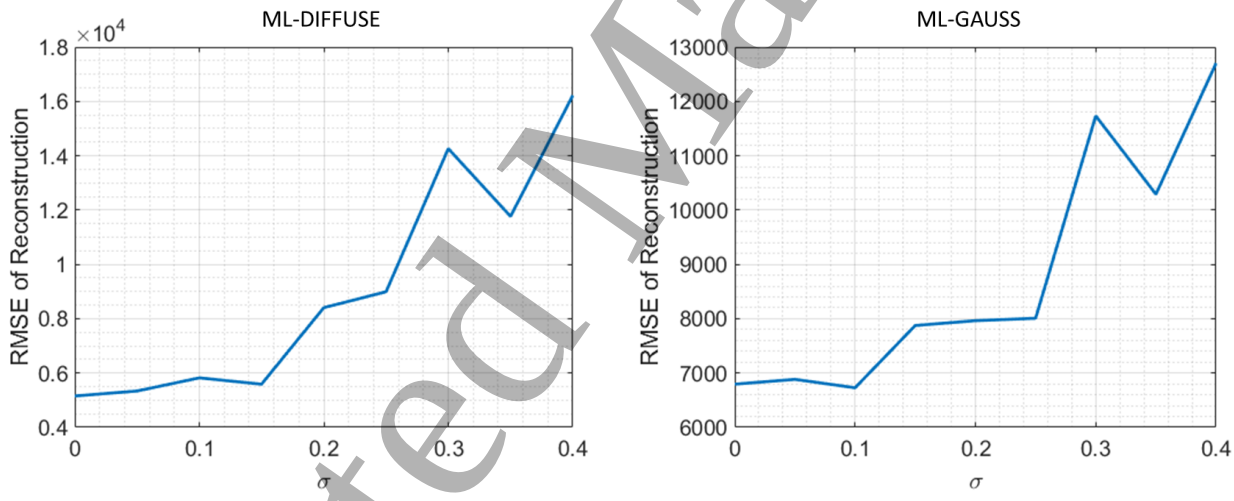

Figure 14: Impact of the measurement uncertainties on the quality of the reconstructions in terms of RMSE between the original phantom and the reconstructions for a quite complex emission pattern.

This method also allows estimating the associated uncertainty, by computing the emitted power within a given region ψ. Figure 15 demonstrates how it is possible to simultaneously estimate both the power and its corresponding uncertainty.

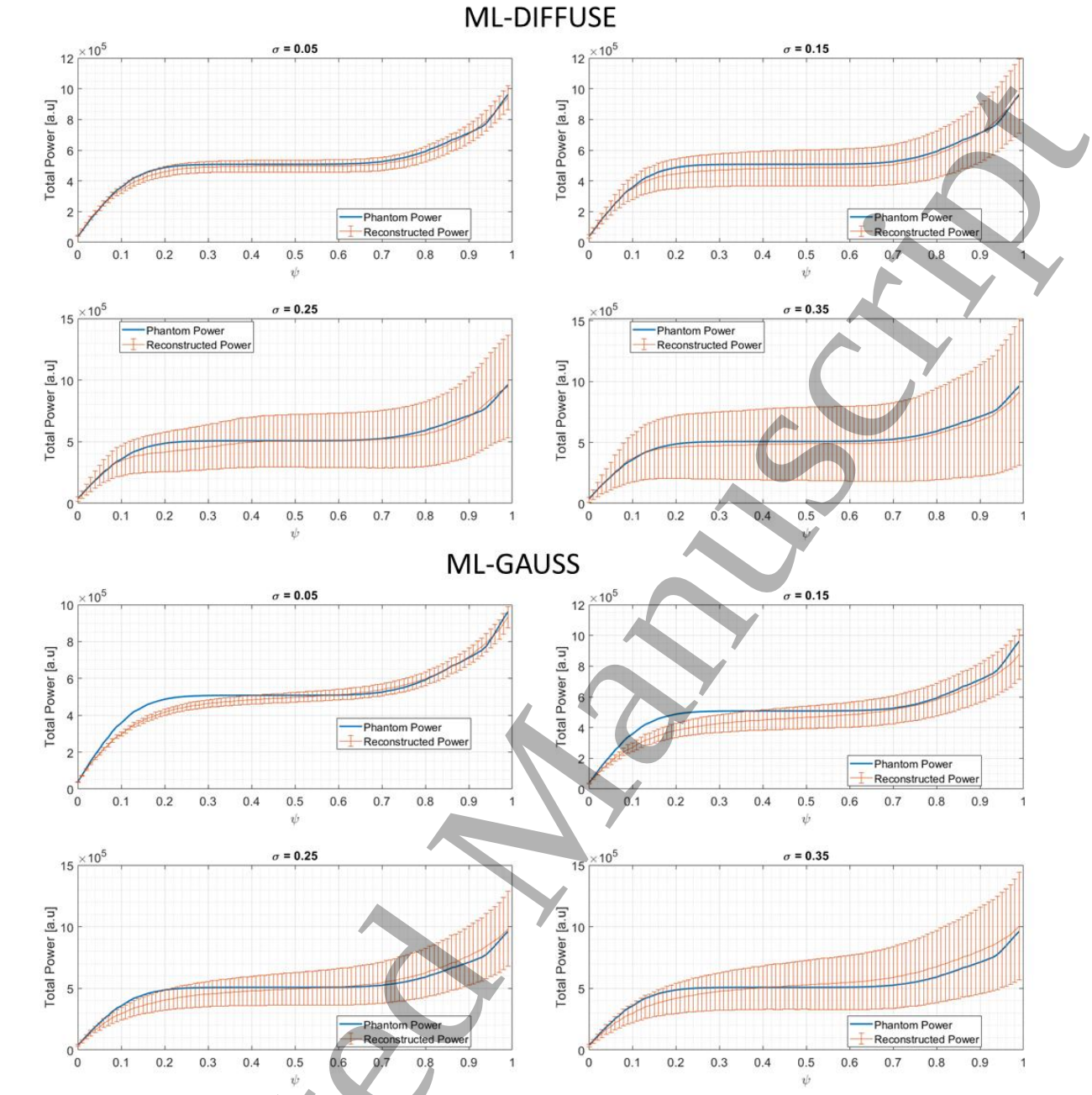

Figure 15: Uncertainties of the reconstructed total emission within a certain normalised radius ψ for different values of the noise added to the synthetic measurements.

It should be noticed that the confidence intervals estimated by the ML-GAUSS method are significantly smaller those of ML-DIFFUSE for all the levels of noise. However the price to be paid is that sometimes the actual emission is slightly outside the ML-GAUSS uncertainty estimates, while this does not occur for ML-DIFFUSE.

4.5 Comparison with other tomographic methods

In Figure 16, some typical cases of radiation patterns encountered on JET are presented. The first case can be associated to impurity accumulation on the low-field side. The second is meant to represent impurity accumulation originating from the divertor. The third corresponds to a radiative ring that can appear during plasma edge cooling. The last is related to divertor radiation observed during seeding experiments; the very narrow emissivity patterns along the invertor legs are inspired by the outputs of simulations such as SOLPS [25]. The same figure shows also a comparison between 4 inversion methods: ML-GAUSS, Tikhonov, MFR,

ML-DIFFUSE. Clearly, the reconstructions depend on the hyper-parameters of each method. Therefore, the reported examples are not to be interpreted as an exhaustive analysis of the differences between the techniques, which is beyond the scope of the present work. This exercise is mainly meant at showing that the developed algorithms produce very reasonable results. Indeed, in all cases, the ML-DIFFUSE method manages to achieve accuracy quite competitive with the best results obtained by the other techniques. This underscores the effectiveness and versatility of the iterative inter-updating filtering, particularly when considering the complex and varied radiation patterns encountered in metallic devices and the fact that the algorithm is self-tuning (not requiring any form of manual intervention). Moreover, it should not be forgotten that both ML-GAUSS and ML-DIFFUSE provide automatically a statically sound estimates of the uncertainties in the emissivity of each voxel. The accuracy of ML-GAUSS is much lower as expected, since it is the only method not utilising the information about the magnetic topology. However, the reconstructions of this algorithm would probably provide very useful information to the control system anyway, given the very short computational time of this alternative version of the code. The fact that the ML-GAUSS fit of the lines of sight is very competitive with the other methods should also not be overlooked. It stresses one more time the limitation of the diagnostic topology.

Phantom	Reconstructions and Errors
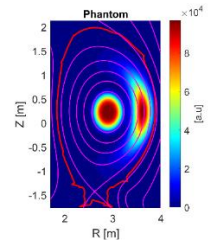	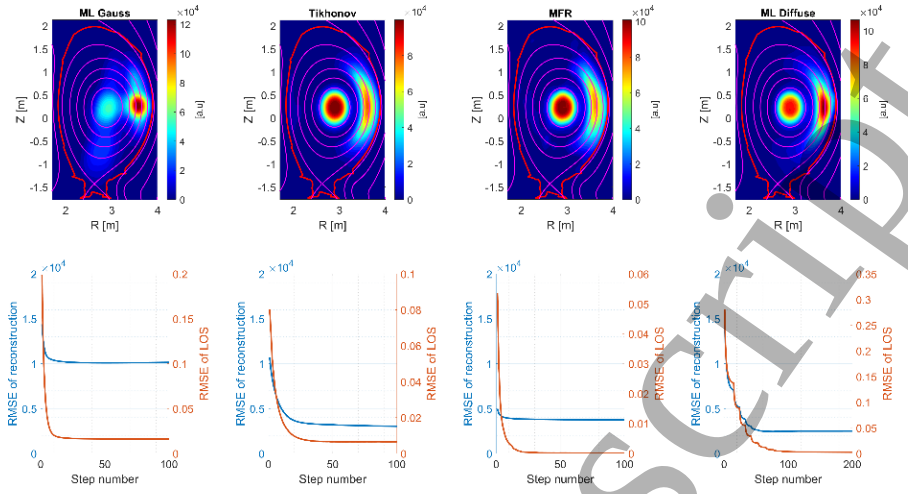
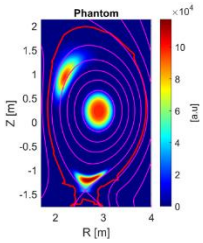	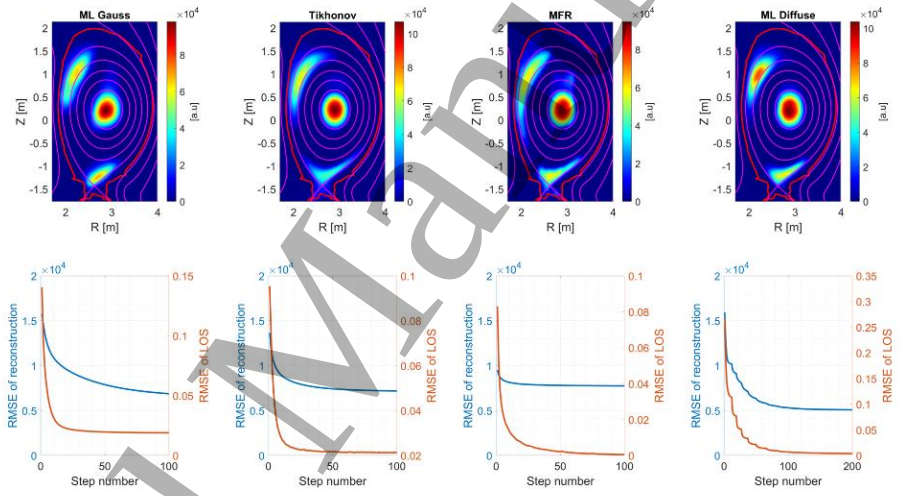
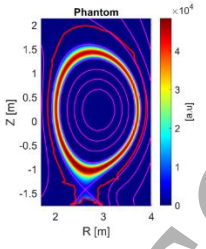	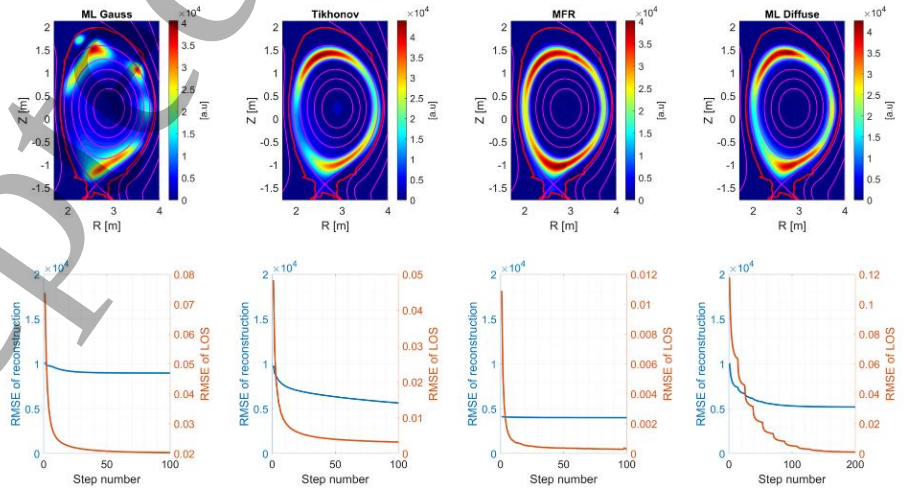

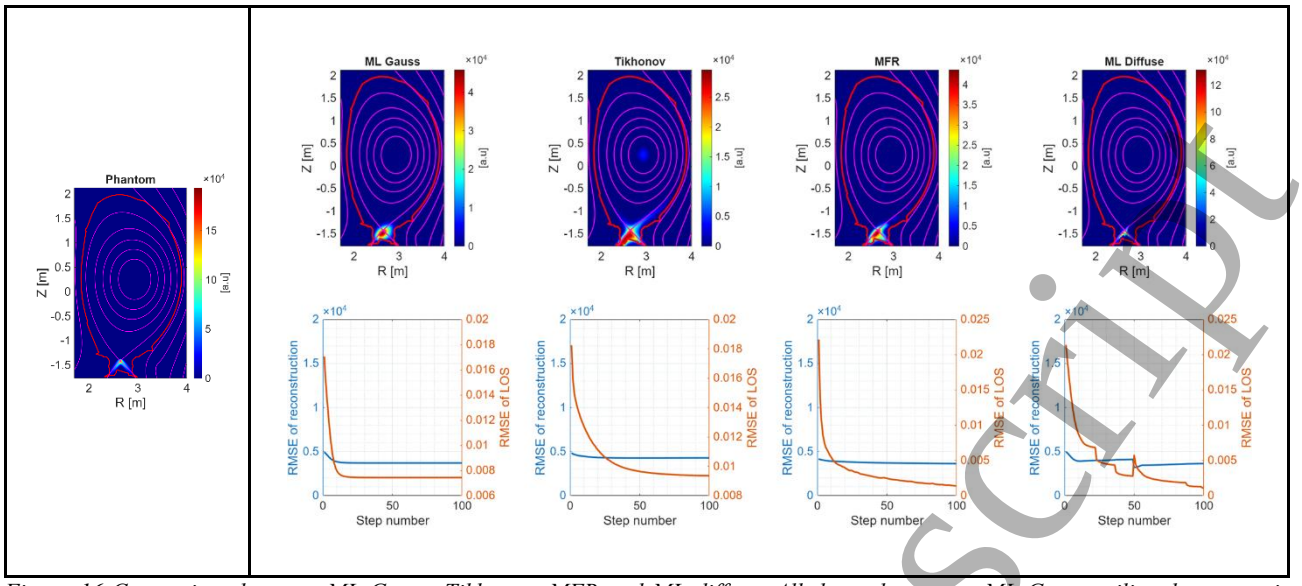

Figure 16:Comparison between ML Gauss, Tikhonov, MFR and ML diffuse. All the codes except ML Gauss utilise the magnetic topology as input.

It is worth showing a detail of the last phantom reconstruction (see Figure 17), from which is possible to notice how small details can be reconstructed with ML-DIFFUSE thanks to the self-tuning strategy.

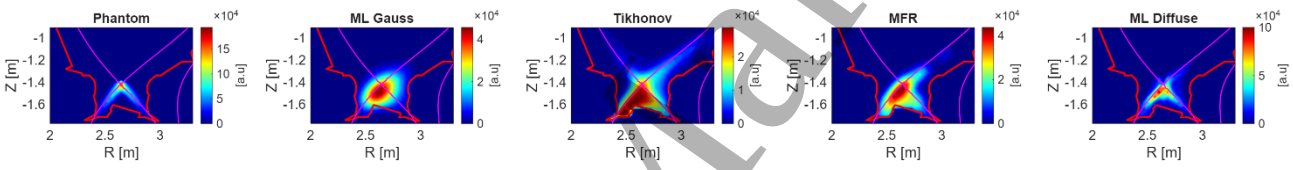

Figure 17: Detail of the divertor for the phantom associated with seeding.

5 Application of the improved ML-EM algorithms to experimental data.

Experimental results have been evaluated with ML-DIFFUSE for various JET pulses. For those particularly relevant to real time feedback control, a comparison between ML-GAUSS and ML-DIFFUSE is presented.

5.1 BOLT Comparison

A first result derived from the experimental data is obtained by comparing the proposed methods with the standard tomographic inversion used for JET bolometry, known as BOLT [26]. Figure 18 shows the reconstructions for four time slices of pulse 97492, obtained with all three methods. The relative error between

ML-DIFFUSE and the standard BOLT remains below 5%, while ML-GAUSS reaches a maximum error of 6.1%.

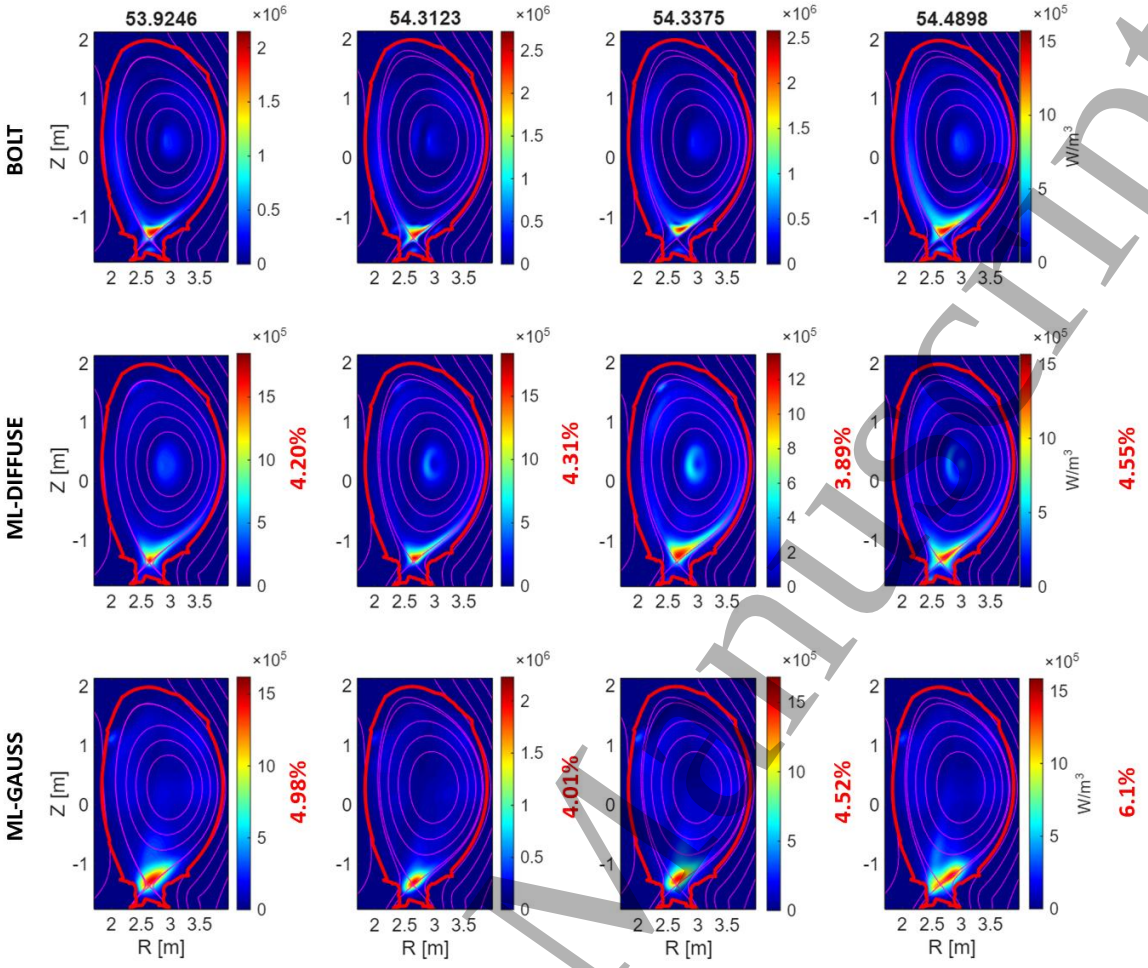

Figure 18: Comparison of the developed methods with the BOLT reconstruction. The values shown in red indicate the relative error with respect to the BOLT tomography and are calculated as the RMSE between the two reconstructions (averaged of all voxels) divided by the maximum value of the emission provided by BOLT.

5.2 Pulses with impurity seeding

In this section, the application of the methodology to the analysis of seeding pulses is presented. Two pulses are considered: the unseeded reference pulse #99464 and the corresponding seeded pulse #99621. Figure 19 shows the key parameters of both discharges. The purpose of seeding is to inject a gas into the plasma, in this case, Neon, in order to reduce the heat load on the divertor by increasing radiation near the X-point. Another major effect of seeding is the change in ELM behaviour, as can be observed from the Be^{1+} line in Figure 19, middle and bottom panels.

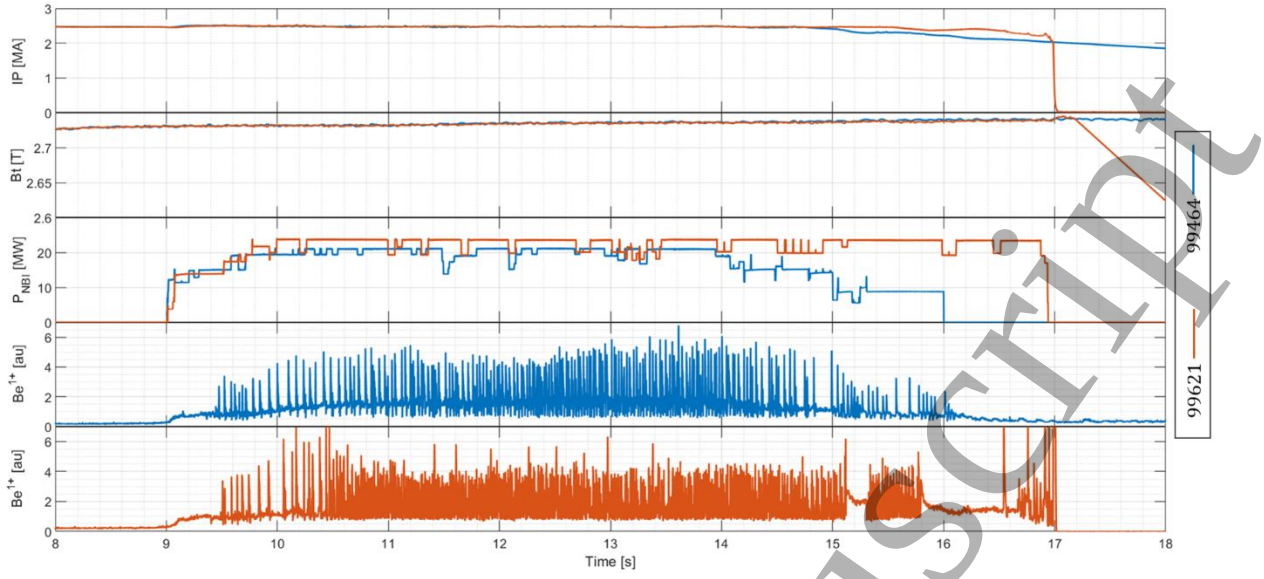

Figure 19: Key parameters of discharges. In blue the parameters of the unseeded #99464 pulse, while in red the parameters of the seeded #99621.

In Figure 20, the tomographic reconstructions obtained with ML-DIFFUSE are shown for both pulses. The main effect of the seeding is an increase in radiation around the X-point. However, this process can also introduce additional impurities, leading to impurity accumulation and eventually to a disruption.

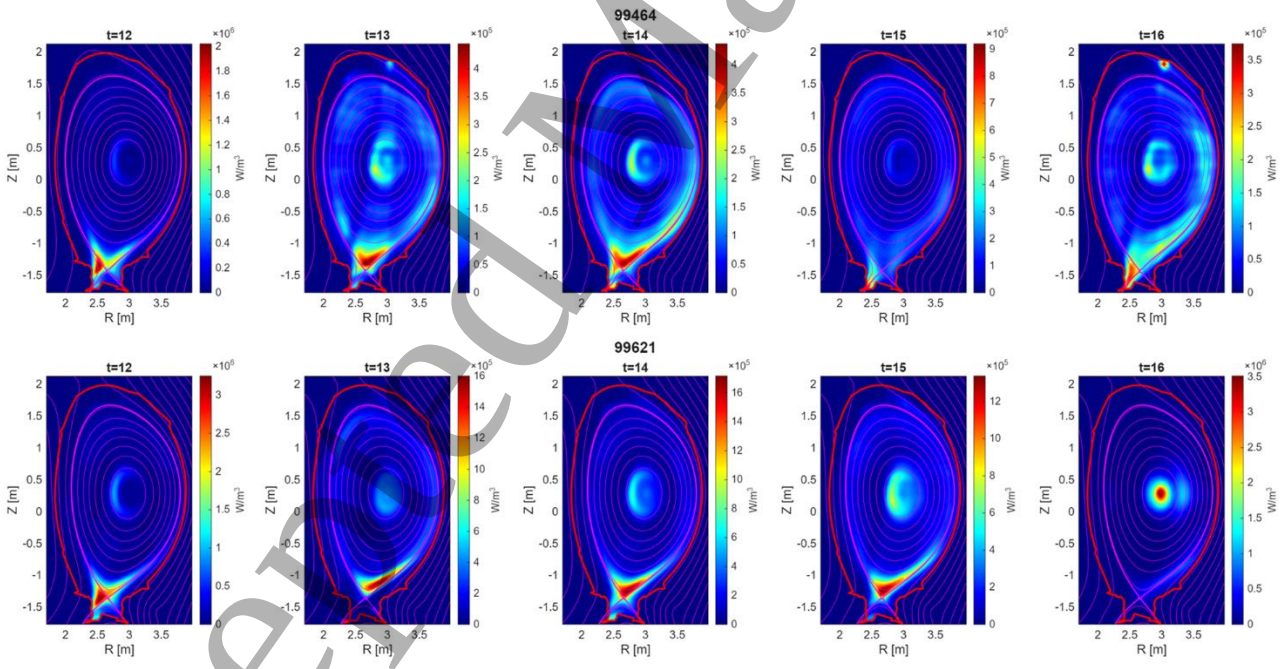

Figure 20: Reconstruction obtained with ML-DIFFUSE for pulses #99464 and #99621.

A better understanding of this phenomenon can be obtained looking to the ELM free phase. In the seeded pulse, two ELM-free phases can be identified: the first between 15.1–15.3 s and the second between 15.7–16.5 s, as shown in Figure 21.

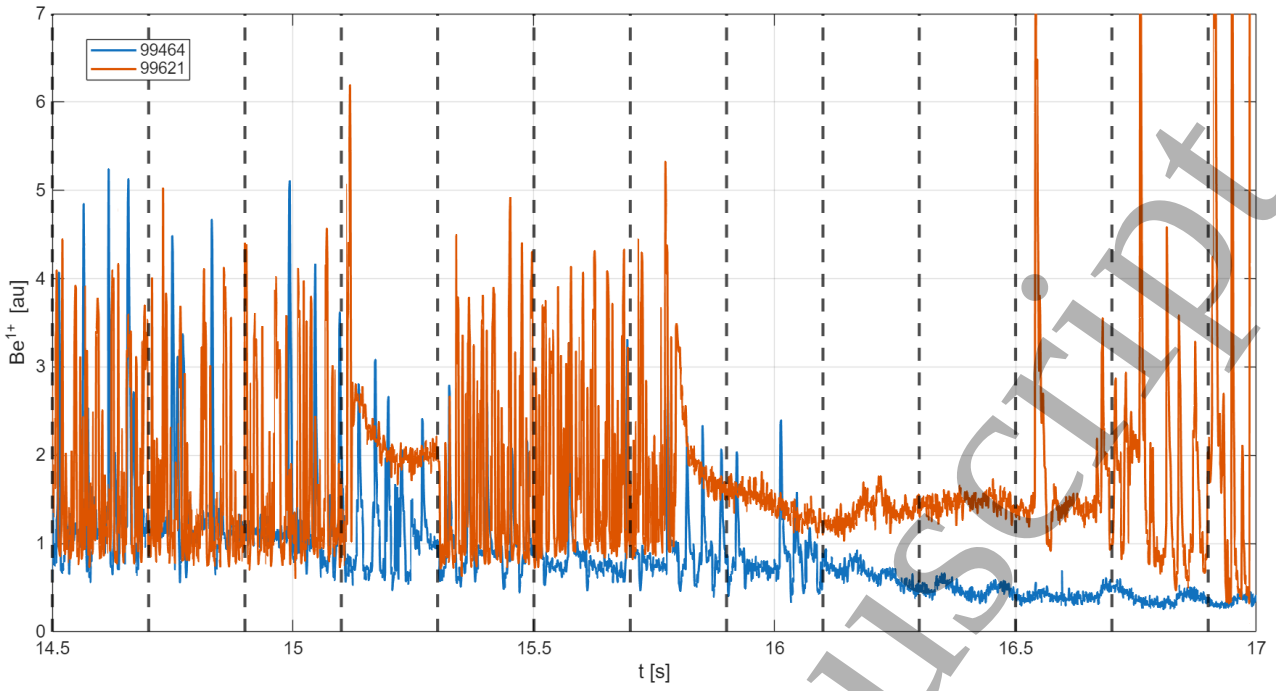

Figure 21:The intensity of the Be signal for both pulses. The dashed vertical line represents the reconstructed time slices

The tomographic reconstructions shown in Figure 22 indicate that the ELM-free phases are strongly associated with enhanced core radiation, likely linked to a higher position of the X-point radiator leading to lower impurity screening, which ultimately leads to a disruption.

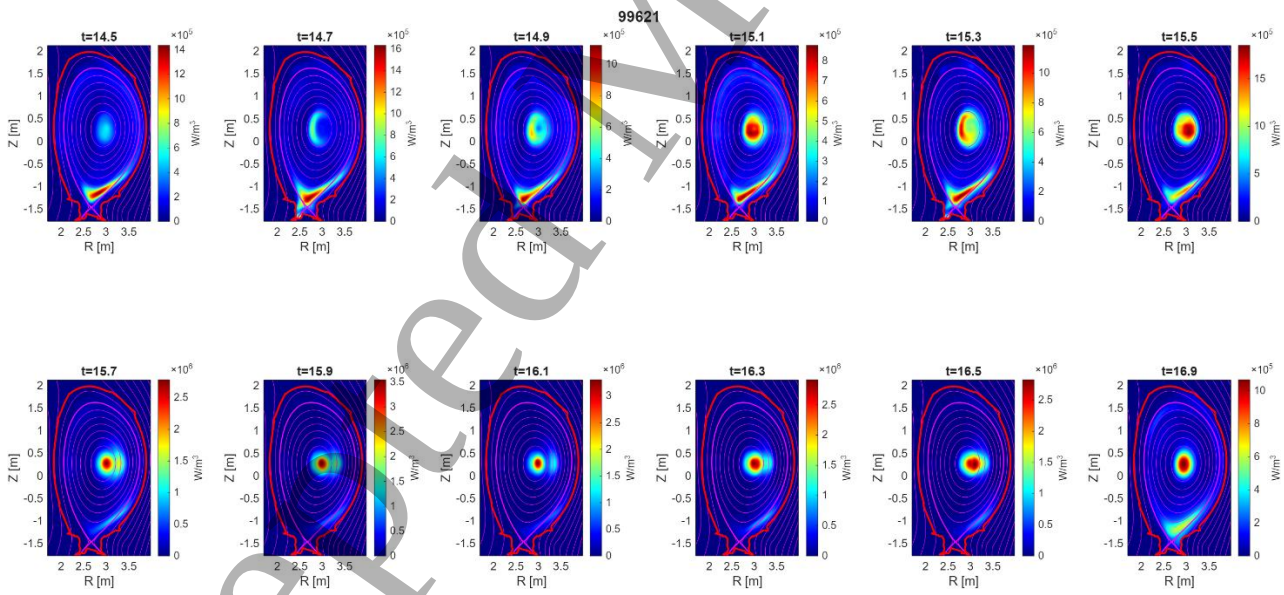

Figure 22:Tomographic inversion of the radiation evolution during an ELM-free phase.

5.3 Pulse 94650 - MARFE

In this pulse a MARFE formation starts moving along the first wall on the high field side, as shown in the visible camera frames reported in Figure 23. Both reconstruction methods give similar results. At the selected times an oscillation of the MARFE from the top to the bottom and back is evident. So, it is possible to track the MARFE from the divertor to the upper part of the vacuum vessel, using ML-GAUSS and with a time resolution determined by the bandwidth of the diagnostic. The blob in the top left corner is an artefact, caused

by the combined effect of toroidally asymmetric emission and the topology of the diagnostic, with the two cameras located in different octants. Since in JET the top left region of the vacuum vessel is observed only by some horizontal lines of sight, when toroidal asymmetries in the radiation occur, the algorithm sometimes erroneously locate some emission in that region, as shown in section 4.3. To interpret the frames of the visible cameras, it should be considered that the diagnostic has a poor time resolution. Consequently if the MARFE moves fast, its image is blurred and much more spatially extended that the actual highly radiative region.

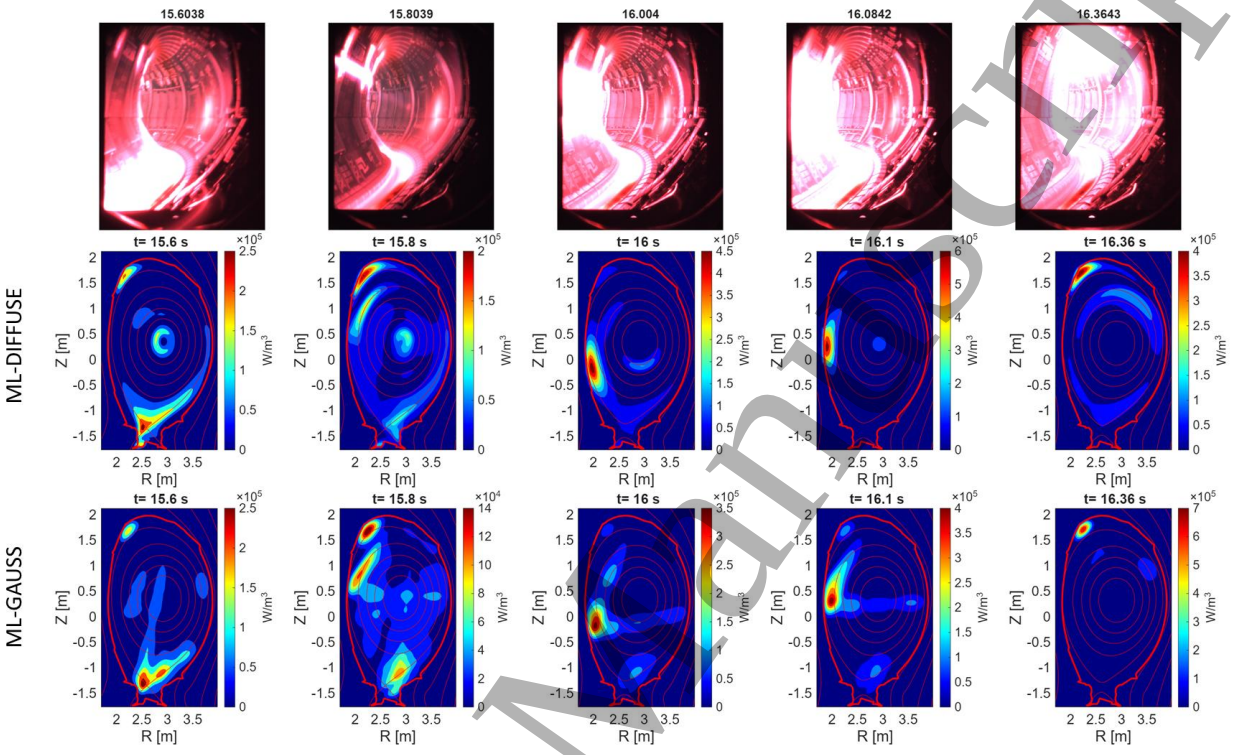

Figure 23:Time evolution of MARFE. (Top) MARFE evolution from visible camera. (Middle)= Image obtained from ML Diffuse. (Bottom) Image obtain from ML Gauss.

5.4 Pulse 96561 Radiative Ring

This example shows how the ML-DIFFUSE method, with the adaptive self-adjusting of the filtering level, produces a more accurate reconstruction, revealing details such as the radiative ring, which ML-GAUSS cannot reconstruct. It is worth mentioning how it has been verified with a specific phantom that the radiative ring can be properly reconstructed by the algorithm when it is present, see Figure 16. Moreover, phantoms with emission in the divertor or in the outer plane have never shown the ring as an artefact. The layout of the diagnostic seems therefore adequate to resolve this specific radiation pattern at least partially. A fast radiative ring collapse in the density limit occurs in the slow ramp-down of pulse 96561. During this ramp-down, the radiation moves from the X-point along the high-field side, forming a poloidal ring, as observed by the visible camera in Figure 24 at 19.373 s and 19.773 s. A comparison shows that the ML-Diffuse approach is able to reconstruct the same behaviour observed by the visible camera in Figure 24, while ML-GAUSS can track the movement of the radiation but it does not reproduce the radiative ring.

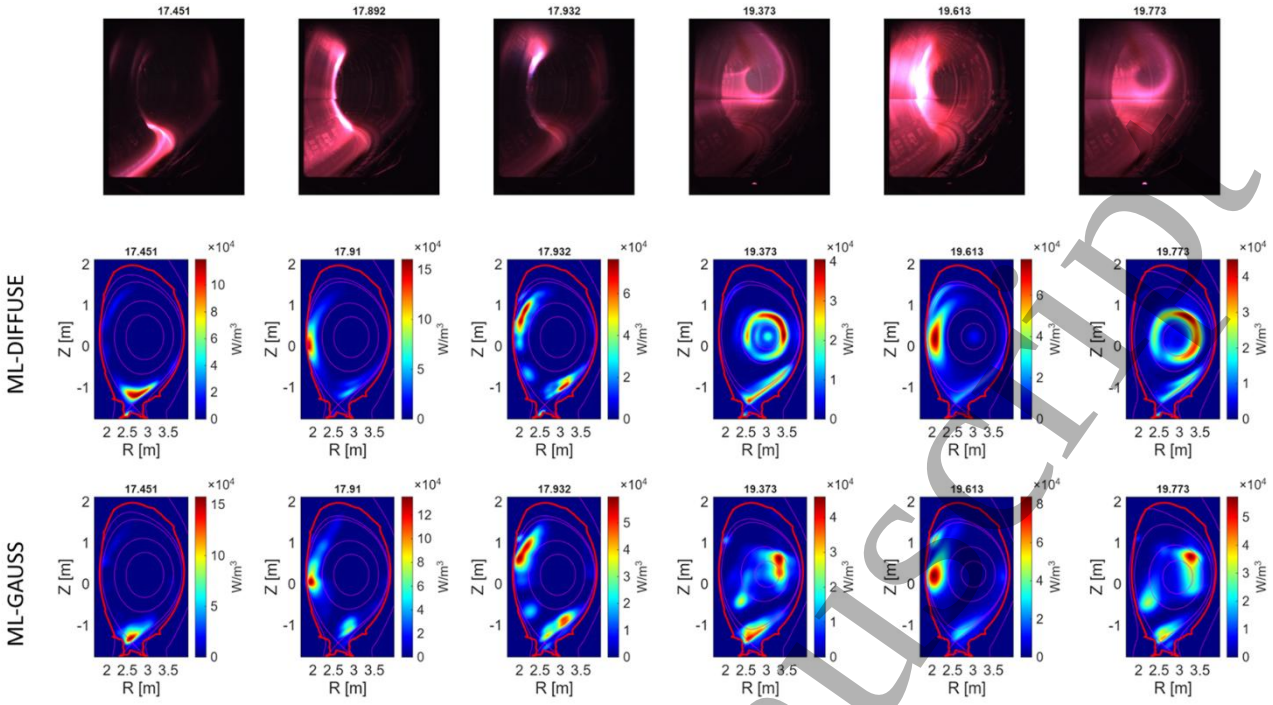

Figure 24: (Top) Visible camera frames for pulse 96561. (Middle) Tomography reconstruction with ML-DIFFUSE.(Bottom) Tomography reconstruction with ML-GAUSS

6 Computational analysis

In this section, an analysis of the required computation times is reported for different grid resolutions, focusing specifically on the reconstruction of a core phantom (in any case representative of what happens also for the other main radiation patterns). The algorithms have been developed in the MATLAB environment, and the performance in terms of computational times has been evaluated on a computer with an Intel Core i5 13600KF @3.5 GHz and 32 GB of RAM. The tests include both the voxels updating (see Subsection 2.1) and the Hadamard product approach (see Subsection 2.2), each for 10 iterations of ML-EM. The initial result highlights a substantial improvement in performance with the adoption of the Hadamard product approach compared to voxels updating. As shown in Figure 25, the advantages of the matrix formulation are evident. Given the inherent nested architecture of the voxels updating algorithm, when considering a typical grid size of 5000 voxels, the element-wise approach delivers a solution that is 2,000 times faster. Moreover, the computational time of the voxels updating with respect to the grid is proportional to $O(n^2)$, while for the matrix approach it scales as $O(n)$. This further underscores the efficiency and scalability of the Hadamard product solution, particularly when dealing with large-scale grids in nuclear fusion scenarios.

The improvement is more evident compared with the typical computational time of different techniques. In [10] the reconstruction time of different algorithms were summarized for grid of about 700 voxels. In this respect, Optimized MFR was the fastest with 0.2s, MFR 1s. With the matrix product solution on a grid of 700 voxels ML-EM takes less than 1ms for 10 iterations, and less than 10s on a million voxels grid. These values should not considered an exhaustive comparison but they are simply meant to indicate that the ML-EM algorithm computation is compatible with real time deployment. Of course to guarantee a deterministic computational time, a requirement of real time codes, the number of iterations must be limited. Just as an example, one could allow a maximum of 20 iterations: in this case the computational time is always below 2 ms and therefore in this respect the algorithm would be compatible with the maximum cycle time of JET, equal to 2 ms. This number of iterations would also typically guarantee sufficient accuracy as shown in Section 4.1.

It should also be considered that the code could be further accelerated, for example by translating it in C++ or even writing it for specific hardware platforms such as GPUs or FPGAs[14]. Moreover, one could start the

iterations with a more realistic first guess than a simple uniform distribution of the emission, as done in all the cases discussed in the present work. Consequently, it is not expected to be prohibitively difficult to develop versions of the ML-GAUSS algorithm compatible with the 2 ms cycle time of JET or of comparable real time networks. Such versions would certainly help control of phenomena such as MARFEs and X-point radiators, by performing feedback schemes using their emitted power particularly in the perspective of future devices. Indeed, reactor level devices will have to work at radiated fractions larger than 90%. In these conditions, an accurate determination of power emitted by MARFEs and X-point radiators will become essential for control[27]. The present day schemes using the line integrals can provide reliable information only about the movement of the emission blobs[28]. With the tomographic inversion, it will also be possible to determine their radiated power and therefore to perform more detailed feedback using this information. For example, it would be possible to assess when an X-point radiator is not emitting enough or whether a MARFE is emitting too much power approaching too risky conditions.

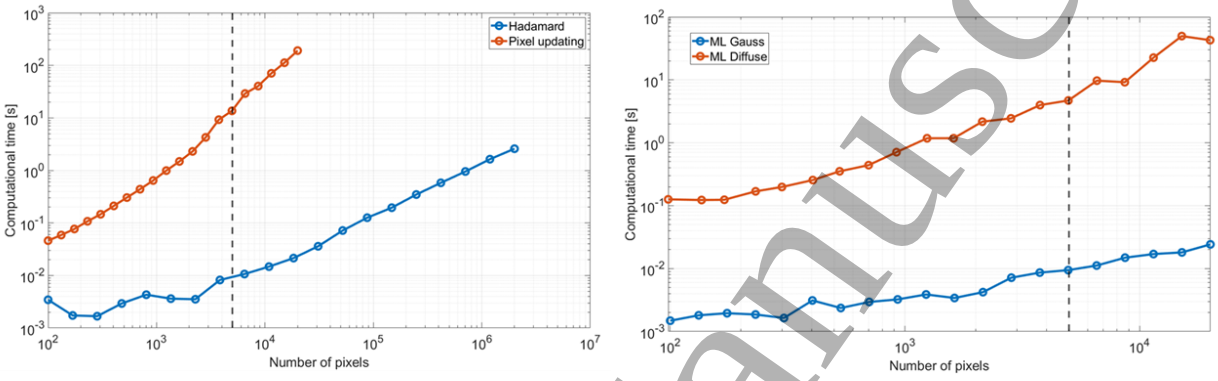

Figure 25: Left: computational times of ML Gauss for the Voxel updating and Hadamard schemes. Right: Computational times for ML Gauss and ML diffuse. The vertical dashed line indicates the number of voxels of the reported results for JET. The computational times reported refer

With regard to the matrix formulation, from Figure 25 it is observed that the running time of the inter updating with Gaussian filtering algorithm increases quite slowly with the number of voxels. This is quite promising in the perspective of deploying this type of inversion approach in the real time networks of larger devices. On the contrary the anisotropic diffusion is strongly dependent on this quantity, because of the need to solve a PDE. Nonetheless, for typical grids used in fusion reactors, the reconstruction would take tens of seconds, making it still suitable for offline reconstructions.

Finally, Figure 26 shows the computational performance of the ML-GAUSS and ML-DIFFUSE as a function of grid size, including the computation of the uncertainty propagation. It can be observed that for ML-GAUSS

with a grids with 1000 voxels, the evaluation time already falls below 50 ms, indicating that with dedicated hardware, performances compatible with real-time deployment can very likely be achieved.

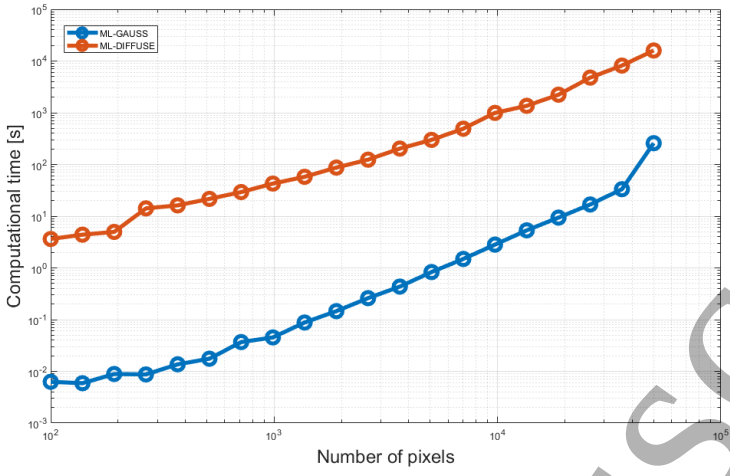

Figure 26: ML-GAUSS and ML-DIFFUSE including the calculation of the confidence intervals

It should be noted that, in the perspective of real time control of the radiation, the computational times achieved by ML-GAUSS are considered already sufficient for many applications. Indeed, depending of the control scheme to be implemented, the real time system typically requires as feedback variable the radiation emitted from a specific region of the cross section (divertor, target plates, core, outer mid plane etc.). Once the reconstruction is available, summing the emission in the relevant pixels to provide this information is typically a submillisecond task. Since the dynamics of most radiation patterns typically present times scales longer than 10 ms, the performances of ML-GAUSS would therefore enable the implementation of a quite wide range of feedback schemes.

7 Conclusions

In this study, we have explored and analysed two inter-updating filtering approaches to tomography for nuclear fusion. Our investigations include systematic tests with phantoms, showing the efficiency and effectiveness of combining inter-updating filtering with the Maximum Likelihood (ML) algorithm. Additionally, Monte Carlo analyses have been conducted to demonstrate the capability of correctly propagating errors even within the inter-updating framework. A notable change from previous works is the modification of the ML updating scheme, resulting in a substantial improvement in computational time. This amelioration renders the approach of the Gaussian filtering suitable to real-time applications. While additional information from magnetic equilibrium could potentially improve reconstruction details, our inter-updating approach with Gaussian filtering possesses the capability of producing reconstructions of reasonable quality quickly, eliminating the need for extra information such as the magnetic field topology. On the other hand, the version of the algorithm with anisotropic diffusion is slower but, by integrating the information about the magnetic equilibrium, provides more accurate solutions.

The adaptive updating of the diffusion parameters makes the procedure equally valid for any type of radiation pattern encountered on JET. It also eliminates the need for human intervention, standardising the procedures and consequently standardising the results. The developed algorithm could therefore be used to provide better training and test sets for deep learning approaches to tomography as those described in [29] [30]. As a result this improved version of the ML-EM could be deployed not only for detailed physical studies but also for building or surveying large databases.

Regarding applications, the new version of the ML-DIFFUSE algorithm opens new horizons to the investigation of practically all the radiative phenomena in tokamaks. Indeed, its accuracy and reasonable

computational times allow its deployment to analyse any instability or operational regime, in which the total radiation plays a fundamental role. In particular the capability of providing routinely the confidence intervals for each pixel of the reconstruction has the potential of contributing significantly to the studies of detachment, impurity seeding and disruption prevention. Of course, given the ill-posed nature of most inversion problems, it is planned also to perform a more systematic comparison with other techniques, such as Gaussian process tomography. Combination and synergy of the developed tools with codes such as SOLPS [25] and the SART algorithm from CHERAB framework would also be extremely useful for the analysis and modelling of experimental data. On the other hand, given the layout of the diagnostic on JET, when important toroidal asymmetries are present in the radiation emission, the bolometric tomography should not be trusted. In some situations, the cause of the asymmetry can be quantified and some remedial actions undertaken. This is the case of localised puffing closed to one of the bolometric cameras, which was analysed in [31].

In terms of technical developments, it could be beneficial to upgrade both ML-GAUSS and ML-DIFFUSE methods by allowing their parameters to be different depending on the location of the voxels in the cross-section. If this could be achieved in a standardised way, without requiring human intervention on a shot-to-shot basis, the benefits would be extremely valuable for both offline and real time applications. Regarding ML-DIFFUSE, it is intended to implement the algorithm using GPU technology, to confirm that the computational times can be reduced and become compatible with real time applications [14].

Acknowledgements

This work has been carried out within the framework of the EUROfusion Consortium, funded by the European Union via the Euratom Research and Training Programme (Grant Agreement No 101052200 — EUROfusion). Views and opinions expressed are however those of the author(s) only and do not necessarily reflect those of the European Union or the European Commission. Neither the European Union nor the European Commission can be held responsible for them.

References

[1] G. Pucella *et al.*, "Onset of tearing modes in plasma termination on JET: The role of temperature hollowing and edge cooling," *Nuclear Fusion*, vol. 61, no. 4, Apr. 2021, doi: 10.1088/1741-4326/ABE3C7.

[2] I. Wyss *et al.*, "Comparison of a fast low spatial resolution inversion method and peaking factors for the detection of anomalous radiation patterns and disruption prediction," 2023, doi: 10.1016/j.fusengdes.2023.113625.

[3] R. Rossi *et al.*, "A systematic investigation of radiation collapse for disruption avoidance and prevention on JET tokamak," *Matter and Radiation at Extremes*, vol. 8, no. 4, Jul. 2023, doi: 10.1063/5.0143193.

[4] P. David, M. Bernert, T. Pütterich, C. Fuchs, S. Glöggler, and T. Eich, "Optimization of the computation of total and local radiated power at ASDEX Upgrade," *Nuclear Fusion*, vol. 61, no. 6, Jun. 2021, doi: 10.1088/1741-4326/abf2e1.

[5] L. Aho-Mantila *et al.*, "Predictions of radiation pattern and in-out asymmetries in the DEMO scrape-off layer using fluid neutrals," *Nuclear Fusion*, vol. 62, no. 5, May 2022, doi: 10.1088/1741-4326/ac4d62.

[6] M. Bernert *et al.*, "The X-Point radiating regime at ASDEX Upgrade and TCV," *Nuclear Materials and Energy*, vol. 34, p. 101376, Mar. 2023, doi: 10.1016/J.NME.2023.101376.

[7] M. Groth *et al.*, "Characterisation of divertor detachment onset in JET-ILW hydrogen, deuterium, tritium and deuterium-tritium low-confinement mode plasmas," *Nuclear Materials and Energy*, vol. 34, 2023, doi: 10.1016/j.nme.2022.101345.

[8] U. Stroth *et al.*, "Model for access and stability of the X-point radiator and the threshold for marfes in tokamak plasmas," *Nuclear Fusion*, vol. 62, no. 7, Jul. 2022, doi: 10.1088/1741-4326/ac613a.

[9] M. Bernert *et al.*, "X-point radiation, its control and an ELM suppressed radiating regime at the ASDEX Upgrade tokamak," *Nuclear Fusion*, vol. 61, no. 2, Feb. 2021, doi: 10.1088/1741-4326/abc936.

[10] M. Odstrcil, J. Mlynar, T. Odstrcil, B. Alper, and A. Murari, "Modern numerical methods for plasma tomography optimisation," *Nucl. Instrum. Methods Phys. Res. A*, vol. 686, pp. 156–161, Sep. 2012, doi: 10.1016/j.nima.2012.05.063.

[11] M. Anton *et al.*, "X-ray tomography on the TCV tokamak," 1996.

[12] K. Moser, A. Bock, P. David, M. Bernert, and R. Fischer, "Gaussian Process Tomography at ASDEX Upgrade with Magnetic Equilibrium Information and Nonstationary Kernels," *Fusion Science and Technology*, vol. 78, no. 8, pp. 607–616, 2022, doi: 10.1080/15361055.2022.2072659.

[13] A. Murari *et al.*, "Investigating the thermal stability of highly radiative discharges on JET with a new tomographic method," *Nuclear Fusion*, vol. 60, no. 4, p. 046030, Mar. 2020, doi: 10.1088/1741-4326/AB7536.

[14] M. Ruiz *et al.*, "Acceleration of an Algorithm Based on the Maximum Likelihood Bolometric Tomography for the Determination of Uncertainties in the Radiation Emission on JET Using Heterogeneous Platforms," *Applied Sciences (Switzerland)*, vol. 12, no. 13, Jul. 2022, doi: 10.3390/app12136798.

[15] A. P. Dempster, N. M. Laird, and D. B. Rubin, "Maximum Likelihood from Incomplete Data Via the EM Algorithm," *J. R. Stat. Soc. Series B Stat. Methodol.*, vol. 39, no. 1, pp. 1–22, Sep. 1977, doi: 10.1111/J.2517-6161.1977.TB01600.X.

[16] D. W. Wilsont, B. M. W. Tsui, and H. H. Barrett, "Noise properties of the EM algorithm: II. Monte Carlo simulations," 1994.

[17] K. Lange and R. Carson, "EM Reconstruction Algorithms for Emission and Transmission Tomography," *Article in Journal of Computer Assisted Tomography*, vol. 1, p. 796, 1984, Accessed: Jan. 31, 2024. [Online]. Available: https://www.researchgate.net/publication/279200328

[18] H. Barrett, D. W. Wilson, and B. M. W. Tsui, "Noise properties of the EM algorithm: I. Theory," 1994.

[19] T. Craciunescu, E. Peluso, A. Murari, and M. Gelfusa, "Maximum likelihood bolometric tomography for the determination of the uncertainties in the radiation emission on JET TOKAMAK," *Review of Scientific Instruments*, vol. 89, no. 5, May 2018, doi: 10.1063/1.5027880.

[20] P. Perona and J. Malik, "Scale-Space and Edge Detection Using Anisotropic Diffusion," 1990.

[21] D. Tschumperlé and R. Deriche, "Vector-Valued Image Regularization with PDEs: A Common Framework for Different Applications." [Online]. Available: http://computer.org/tpami/archives.htm

[22] J. Qi, "A unified noise analysis for iterative image estimation," 2003.

[23] T. Craciunescu, G. Bonheure, V. Kiptily, A. Murari, I. Tiseanu, and V. Zoita, "A comparison of four reconstruction methods for JET neutron and gamma tomography," *Nucl. Instrum. Methods Phys. Res. A*, vol. 605, no. 3, pp. 374–383, Jul. 2009, doi: 10.1016/j.nima.2009.03.224.

[24] A. Huber *et al.*, "Improved radiation measurements on JET-First results from an upgraded bolometer system", doi: 10.1016/j.jnucmat.2007.01.124.

[25] E. Kaveeva *et al.*, "SOLPS-ITER drift modelling of JET Ne and N-seeded H-modes," *Nuclear Materials and Energy*, vol. 28, Sep. 2021, doi: 10.1016/j.nme.2021.101030.

[26] L. C. Ingesson *et al.*, "SOFT X RAY TOMOGRAPHY DURING ELMs AND IMPURITY INJECTION IN JET."

[27] A. Huber *et al.*, "The radiated power limit in impurity seeded JET-ILW plasmas," *Nuclear Materials and Energy*, vol. 33, Oct. 2022, doi: 10.1016/j.nme.2022.101299.

[28] T. O. S. J. Bosman *et al.*, "X-point radiator control and its dynamics in ASDEX Upgrade and JET deuterium-tritium discharges," *Nuclear Fusion*, vol. 65, no. 1, Jan. 2025, doi: 10.1088/1741-4326/ad99cc.

[29] R. Rossi, M. Gelfusa, and A. Murari, "On the potential of physics-informed neural networks to solve inverse problems in tokamaks," 2023, doi: 10.1088/1741-4326/ad067c.

[30] F. A. Matos, D. R. Ferreira, and P. J. Carvalho, "Deep learning for plasma tomography using the bolometer system at JET," *Fusion Engineering and Design*, vol. 114, pp. 18–25, Jan. 2017, doi: 10.1016/J.FUSENGDES.2016.11.006.

[31] E. Peluso *et al.*, "Correction of JET bolometric maximum likelihood tomography for local gas puffing," *Plasma Phys. Control. Fusion*, vol. 65, no. 7, p. 075003, May 2023, doi: 10.1088/1361-6587/ACCD1C.